# Expanding the Cage of 2D Bromide Perovskites by Large A-Site Cations

Xiaotong Li, Shelby Cuthriell, Ashanti Bergonzoni, Hao Dong, Boubacar Traore, Constantinos Stoumpos, Peijun Guo, Jacky Even, Claudine Katan, Richard Schaller, et al.

# Expanding the Cage of 2D Bromide Perovskites by Large A-site Cations

Xiaotong Li,[†] Shelby A. Cuthriell,[†] Ashanti Bergonzoni,[‖] Hao Dong,[‡] Boubacar Traoré,[§] Constantinos C. Stoumpos,[▽] Peijun Guo,[‡] Jacky Even,[‖] Claudine Katan,[§] Richard D. Schaller,[†,◊] and Mercouri G. Kanatzidis[*,†]

[†]Department of Chemistry, Northwestern University, 2145 Sheridan Road, Evanston, Illinois 60208, United States
[‖]Univ Rennes, INSA Rennes, CNRS, Institut FOTON, UMR 6082, Rennes F-35000, France
[‡]Department of Chemical and Environmental Engineering, Yale University, New Haven, Connecticut 06511, United States
[§]Univ Rennes, ENSCR, INSA Rennes, CNRS, ISCR (Institut des Sciences Chimiques de Rennes), UMR 6226, Rennes F-35000, France
[▽]Department of Materials Science and Technology, Voutes Campus, University of Crete, Heraklion GR-70013, Greece
[◊]Center for Nanoscale Materials, Argonne National Laboratory, 9700 South Cass Avenue, Lemont, Illinois 60439, United States

## Abstract

Two-dimensional (2D) halide perovskites have outstanding optoelectronic properties, and they feature a variety of organic cation spacers and cage A-site cations that can be incorporated into their structures. It has recently been reported that the Goldschmidt tolerance factor can be relaxed and expanded in iodide 2D perovskites. Bromide 2D perovskites, whose multilayer structures and optical properties are much less studied, provide a great platform for studying structure–property relationships for 2D perovskites with large A-site cations. Herein, we report the synthesis and structure of three new 2D bromide perovskites—$(BA)_2(MHy)_2Pb_3Br_{10}$ (BA, butylammonium; MHy, methylhydrazinium), $(BA)_2(EA)_2Pb_3Br_{10}$ (EA is ethylammonium), and $(BA)_2(DMA)Pb_2Br_7$ (DMA is dimethylammonium). We compared them with other 2D perovskites with different A-site cations but with the same spacer and layer thickness. Single-crystal structures show that the Pb-Br bonds are elongated to accommodate the large A-site cations. Additionally, the octahedra in $(BA)_2(MHy)_2Pb_3Br_{10}$ and $(BA)_2(EA)_2Pb_3Br_{10}$ are highly distorted, and their different stacking

patterns of the inner and outer layers lead to the formation of the n = 3 phase. Density functional theory calculations show that 2D perovskites with larger A-site cations (e.g. DMA, MHy and EA) have smaller band dispersions and larger effective masses than those with $Cs^+$ and MA. $(BA)_2(MHy)_2Pb_3Br_{10}$ also exhibits one of the largest Rashba splitting in the literature. Structures with large cage cations also exhibit a high bandgap within the same layer number and short photoluminescence (PL) lifetimes. Temperature- and power-dependent PL measurements reveal that the broad shoulder in the PL peak originates from the trap states.

## Introduction

Halide perovskites have attracted extensive research interest for applications in optoelectronic devices[1-3] owing to their outstanding physical properties.[4-6] The most extensively studied three-dimensional (3D) halide perovskites have the general formula $AMX_3$, where A is a +1 cation, M is a +2 metal, and X is a halide.[7, 8] The choice of the A-site cation can be guided by the Goldschmidt tolerance factor, $t = (r_A + r_X)/[\sqrt{2}(r_M + r_X)]$, where $r_A$, $r_M$ and $r_X$ are the effective radii of $A^+$, $M^{2+}$, and $X^-$ ions, respectively.[9, 10] When $0.8 < t < 1$, the proper perovskite phase can form, but when $t$ is outside the range, a non-perovskite phase is formed. For most reported main-group halide perovskites, A is $Cs^+$, $CH_3NH_3^+$ (MA), or $HC(NH_2)_2^+$ (FA), where M is $Pb^{2+}$, $Sn^{2+}$, or $Ge^{2+}$, and X is $I^-$, $Br^-$, or $Cl^-$.[7, 8] Extensive research has been devoted to mixing A-site cations of different sizes to preserve the perovskite structure and, in turn, improve the efficiency as well as the stability of perovskite solar cells.[11, 12] However, these large A-site cations (e.g. dimethylammonium and guanidinium) by themselves cannot stabilize the 3D perovskite structures. Usually, a large cation ($t > 1$) is balanced with a small cation ($t < 0.8$) or one within the optimal range ($0.8 < t < 1$). There is crystallographic[13, 14] and solid-state nuclear magnetic resonance (NMR)[15] evidence that some amount of a large cation can be accommodated within the structure.[14]

Recently, large A-site cations have been incorporated into 3D perovskite lattices, and their structures have been characterized by single-crystal X-ray diffraction. For example, in 2019, Huang *et al.* reported that halogenated-methylammonium may form 3D halide perovskite nanocrystals; they also reported the single-crystal structure of $FMAPbBr_3$ ($FMA = CH_2FNH^{3+}$), which adopts the space group of $Im\bar{3}m$ at 153 K.[16] In 2020, Zhang *et al.* reported the structure of $(CH_3PH_3)SnBr_3$, which adopts the *Pc* space group at room temperature and goes through two phase transitions at higher temperatures.[17] At 333 K, it adopts the orthorhombic space group of $Pna2_1$,

and at 383 K, it goes to the cubic spacer group of $Pm\bar{3}m$.[17] Recently, Mączka *et al.* reported that methylhydrazinium (MHy) can serve as A-site cation in $MHyPbBr_3$ and $MHyPbCl_3$, both of which adopt the $P2_1$ space group at room temperature and go through phase transitions at higher temperatures.[18, 19] The room temperature structures of $MHyPbBr_3$ and $MHyPbCl_3$ are highly distorted to accommodate the large cation. Interestingly, MHy can also serve as a spacer cation in 2D perovskites $(MHy)_2PbI_4$ and $(MHy)_2PbBr_4$, where the octahedra are not tilted (Pb-X-Pb angles close to 180°), and the interlayer distances are small, leading to smaller bandgaps than those of the other n = 1 structures of the same halide.[20, 21]

The 2D perovskites are derived from the 3D analogues by cutting along the (100) plane and inserting organic cations between them. The most prominent class is the Ruddlesden-Popper (RP) perovskites with the general formula $(A')_2A_{n-1}M_nX_{3n+1}$ (where A' is the large spacing cation and A is the cage cation, as in $AMX_3$ above). The value of n refers to the thickness of the layers in units of $[MX_{6/2}]^-$ octahedra. In 2D perovskites, it appears that the tolerance factor can be further extended compared to that in 3D structures. For example, isopropylammonium (IPA)[22] and ethylammonium (EA)[23] can serve as both the A-site cage cation and spacer cation in $(IPA)_2(IPA)Sn_2I_7$ and $(EA)_2(EA)_2Pb_3X_{10}$ (X = Br or Cl), respectively. However, there is a growing number of examples where the spacer cations and cage cations are different. Fu *et al.* reported the relaxation of the tolerance factor in 2D perovskites, where different A-site cations were incorporated into 2D perovskites.[24] We further studied the structure–property relationships in the n = 2 perovskites $(BA)_2(A)Pb_2I_7$[25] (BA = butylammonium, A = methylammonium (MA), formamidinium (FA), dimethylammonium (DMA), guanidinium (GA)), and n = 3 phase $(BA)_2(EA)_2Pb_3I_{10}$[26]. The latter was studied as an antiferroelectric and X-ray detector.[27, 28] The large

A-site cation EA can also improve the ferroelectric performance of the 2D perovskite using 4-aminomethyl-1-cyclohexanecarboxylate (*t*-ACH) as the spacer.[29]

Based on our experience and reported literature,[30, 31] the bromide perovskites have the largest structural flexibility. On the one hand, because the Pb-Br bond length is in between Pb-I and Pb-Cl, the bromide structure has moderate cage space. On the other hand, Br has moderate electronegativity between I and Cl, so the bromide structures can form reasonably strong hydrogen bonding with the organic cations that enables various types of interesting structures. However, the structure–property relationships of bromide 2D perovskites are less studied compared with those of iodides. Here, we report three new bromide 2D perovskites with large A-site cations: $(BA)_2(MHy)_2Pb_3Br_{10}$, $(BA)_2(EA)_2Pb_3Br_{10}$, and $(BA)_2(DMA)Pb_2Br_7$. We compared their structures and properties with those of other bromide 2D perovskites with the same layer number. The effective radii of the cations used in this study are listed in Table 1. We found that in addition to cage expansion and negative pressure imposed by the large A cation octahedral distortion, Pb off-centering also occurs. Such a unique stacking pattern of distorted and undistorted layers may be the reason why only one of the layer numbers (n = 2 or n = 3) can be stabilized for each A cation. Density functional theory (DFT) calculations suggest that as the size of the A-site cation increases, the band dispersion decreases and the effective mass increases. The 2D perovskites with larger A-site cations exhibit higher bandgaps and shorter PL lifetimes than those with small A cations. Low-frequency Raman spectra suggest that their lattice is very soft and anharmonic, and the phonon modes shift to lower frequencies with the increase in the size of the A cation.

## Experimental Section

The starting materials $PbBr_2$ (98%), methylamine hydrochloride (98%), formamidine acetate (99%), dimethylamine hydrochloride (99%), methylhydrazine (98%), ethylammonium chloride

(98%), hydrobromic acid (48 wt % in $H_2O$, distilled, stabilized, 99.95%), and hypophosphorous acid solution (50 wt % in $H_2O$) were purchased from Sigma-Aldrich and used as received.

**Synthesis**

$(BA)_2(MA)Pb_2Br_7$[32] and $(BA)_2(MA)_2Pb_3Br_{10}$[33] were synthesized according to methods reported elsewhere. We note that the methods reported here only give rise to small single crystals (< 1mm). For centimeter size single crystals, please refer to methods reported in the literature.[33-35]

**$(BA)_2(Cs)Pb_2Br_7$.** 1.5 mmol $PbBr_2$ (550.5 mg) and 1 mmol cesium nitrate (194.9 mg) were dissolved in 9 mL of concentrated HBr solution under heating and continuously stirred at 120 °C. Then, 4 mmol (396 μL) butylamine (BA) was added to 1 mL of concentrated aqueous $H_3PO_2$ solution in a separate vial under stirring. The neutralized BA solution was added to the HBr solution under stirring until a clear solution was obtained. Then, the hot plate was turned off, and the solution was cooled to room temperature. The light-yellow crystals settled at the bottom of the vial after 24h and were isolated by suction filtration followed by drying under vacuum for 30 min. Yield: 389.6 mg, 31.0% based on total Pb.

**$(BA)_2(FA)Pb_2Br_7$.** 3 mmol $PbBr_2$ (1101 mg) and 2 mmol formamidine (FA) acetate (208.2 mg) were dissolved in 6 mL of concentrated HBr solution under heating and stirring at 120 °C. Then, 2 mmol (198 μL) butylamine (BA) was added to 1 mL of concentrated aqueous $H_3PO_2$ solution in a separate vial under stirring. The neutralized BA solution was added to the HBr solution under stirring until a clear solution was obtained. Then, the hot plate was turned off, and the solution was cooled to room temperature. The light-yellow crystals settled at the bottom of the vial after 24h and were isolated by suction filtration followed by drying under vacuum for 30 min. Yield: 488.6 mg, 41.6% based on the total Pb.

**$(BA)_2(DMA)Pb_2Br_7$.** 4 mmol $PbBr_2$ (1468 mg) and 2 mmol dimethylamine (DMA) hydrochloride (163.2 mg) were dissolved in 5 mL of concentrated HBr solution under heating and stirring at 120 °C. First, 1 mmol (99 μL) butylamine (BA) was added to 1 mL of concentrated aqueous $H_3PO_2$ solution in a separate vial under stirring. The neutralized BA solution was added to the HBr solution under stirring until a clear solution was obtained. Then, the hot plate was turned off, and the solution was cooled to room temperature. The light-yellow crystals settled at the bottom of the vial after 24h and were isolated by suction filtration followed by drying under vacuum for 30 min. Yield: 214.7 mg, 18.4% based on total Pb.

**$(BA)_2(EA)_2Pb_3Br_{10}$.** A total of 6 mmol of $PbBr_2$ (2202 mg) and 4 mmol ethylamine (EA) hydrochloride (326.2 mg) was dissolved in 6 mL of concentrated HBr solution under heating and stirring at 120 °C. Then, 2 mmol (198 μL) butylamine (BA) was added to 1 mL of concentrated aqueous $H_3PO_2$ solution in a separate vial under stirring. The neutralized BA solution was added to the HBr solution under stirring until a clear solution was obtained. Then, the hot plate was turned off, and the solution was cooled to room temperature. The light-yellow crystals settled at the bottom of the vial after a day and were isolated by suction filtration followed by drying under vacuum for 30 min. Yield: 1152 mg, 34.7% based on total Pb.

**$(BA)_2(MHy)_2Pb_3Br_{10}$.** 6 mmol $PbBr_2$ (2202 mg) was dissolved in 5 mL of concentrated HBr solution under stirring. Methylhydrazine (MHy, 4 mmol, 210 μL) was added to the solution. First, 1 mmol (99 μL) butylamine (BA) was added to 1 mL of concentrated aqueous $H_3PO_2$ solution in a separate vial under stirring. The neutralized BA solution was added to the HBr solution under heating and stirring at 120 °C until a clear solution was obtained. Then, the hot plate was turned off, and the solution was cooled to room temperature. The light-yellow crystals settled at the

bottom of the vial after 24h and were isolated by suction filtration followed by drying under vacuum for 30 min. Yield: 701.2 mg, 21.1% based on total Pb.

More details about the characterizations and physical measurements can be found in the Supporting Information.

## Results and Discussion

### Synthesis

$(BA)_2(MA)Pb_2Br_7$ and $(BA)_2(MA)_2Pb_3Br_{10}$ were synthesized according to previously reported methods.[32, 33] The other compounds were synthesized using a similar solution method by tuning the ratio between the BA spacer and $PbBr_2$. For example, for $(BA)_2(DMA)Pb_2Br_7$, we dissolved stoichiometric ratio of the $PbBr_2$ (4 mmol) and DMA (2 mmol) in concentrated HBr at 120 °C; then, we added ¼ of the stoichiometric ratio of BA (1 mmol) to the solution. After a clear solution was obtained, it was cooled directly to room temperature because there was no second phase that can precipitate out. The sub-stoichiometric ratio was used to avoid the formation of n = 1 phase $(BA)_2PbBr_4$, which is less soluble in an aqueous acidic solution because it has a larger organic molar fraction. By reducing the amount of BA, a more soluble n = 2 phase precipitated out. For $(BA)_2(MHy)_2Pb_3Br_{10}$, ¼ of the stoichiometric ratio of BA was used for the same reason, while for $(BA)_2(EA)_2Pb_3Br_{10}$, ½ of the stoichiometric ratio of BA was added. A remarkable synthetic aspect that we observed is that the MHy cation is only present in its +1 form ($CH_3NH_2NH_2^+$), and it does not doubly protonate to form the +2 dication ($CH_3NH_2NH_3^{2+}$) despite the presence of a large excess of strong acid present. It is likely that both the +1 and +2 species exist in solution in equilibrium and that the layered perovskite is formed by "selecting" the monocation that satisfies the charge

balance requirements. Notably, although we tuned the ratio of BA from 1/12 to ½ of the stoichiometric ratio (BA:EA:Pb from 1:12:18 to 1:2:3), we did not obtain a higher layer number than n = 2 for $(BA)_2(DMA)Pb_2Br_7$. For $(BA)_2(MHy)_2Pb_3Br_{10}$ and $(BA)_2(EA)_2Pb_3Br_{10}$, no evidence for the existence of other layer numbers has been found, which we discuss in detail below.

The powder X-ray diffraction (PXRD) patterns for the n = 3 and n = 2 phases are shown in Figure S1. The PXRD patterns of the new structures ($(BA)_2(DMA)Pb_2Br_7$, $(BA)_2(MHy)_2Pb_3Br_{10}$, and $(BA)_2(EA)_2Pb_3Br_{10}$) are similar to those reported for the same layer number (e.g., $(BA)_2(MA)Pb_2Br_7$ and $(BA)_2(MA)_2Pb_3Br_{10}$). However, the peaks shift to lower angles because of the larger d-spacing caused by the large A-site cations (see below). For the n = 2 phases, there are two low-angle peaks below $2\theta \sim 14°$. For the n = 3 phase, there are three equally spaced peaks, which are characteristic of 2D perovskites, and the absence of other peaks suggests that there is no second phase.

**Description of the Crystal structures**

**n = 3 phases**

The two new n = 3 phases, $(BA)_2(MHy)_2Pb_3Br_{10}$ and $(BA)_2(EA)_2Pb_3Br_{10}$, were refined in the noncentrosymmetric space group of *Cc* (Figure 1), with crystal and refinement data shown in Table 2 and more detailed crystallographic data shown in Table S1-S6. However, their unit cells were different. $(BA)_2(EA)_2Pb_3Br_{10}$ adopts more isotropic in-plane unit cell parameters with similar *b* and *c* axes ($b \approx c \approx \sqrt{2} \times 2 \times Pb - Br$), which is common in most 2D perovskites[36, 37]. By contrast, the unit cell parameter of $(BA)_2(MHy)_2Pb_3Br_{10}$ is anisotropic, $b \approx 2 \times Pb - Br$ while $c \approx 4 \times Pb - Br$, similar to the $(GA)(MA)_nPb_nI_{3n+1}$ (GA = guanidinium) phases.[38] For $(BA)_2(MHy)_2Pb_3Br_{10}$, the octahedra lying on the surface of the layers (outer layer) are uniform, while the octahedra in the

inner part of the layers are highly distorted. We calculated the distortion index (D) and bond angle variance ($\sigma^2$) using equations (1) and (2) available in Vesta software (Table 3)[39], which is a measure of the extent to which each Pb-Br bond length ($l_i$) and Br-Pb-Br bond angle ($\theta_i$) deviate from the average value ($l_{av}$ and 90°) within each individual octahedron. The distortion index increases with increasing size of the A-site cation, as shown in Figure 2, which suggests the individual octahedron is more distorted with larger cage cations. For $(BA)_2(MHy)_2Pb_3Br_{10}$, the inner layer has a larger D and $\sigma^2$ than the outer layers, which is more obvious for $\sigma^2$ because some of the Br-Pb-Pb angles are far from 90° (*e.g.*, 80° or 100°). Looking at the top view for the inner and outer layers separately (Figure S2), we can see that the inner layer octahedra are highly distorted, and the Pb atoms are clearly off-centered, while the outer layer octahedra are more uniform and their Pb-Br-Pb angles are close to 180°. As shown in Figure S2b, the adjacent four Pb atoms form a square, and the unit cells of most 2D perovskites cross the diagonals of the square, as indicated by the purple lines. However, for the inner layer, the adjacent four Pb atoms form an irregularly shaped void and the four adjacent diagonals have two very different values (Figure S2a). From the side view (Figure 1a), the structure adopts an *A-B-A* stacking pattern. This stacking pattern cannot exist in an even layer number, which may explain why the n = 2 phase cannot be synthesized, despite systematic synthetic attempts. For $(BA)_2(EA)_2Pb_3Br_{10}$, the outer layer was more distorted than the inner layer, as shown in Table 3. However, it also adopts the *A-B-A* stacking pattern, and we have only succeeded in synthesizing the n = 3 phase so far. Notably, in the iodide analogue $(BA)_2(EA)_2Pb_3I_{10}$[26] and the bromide structure with just EA, $(EA)_2(EA)_2Pb_3Br_{10}$[23], there are no other members with n≠3 observed thus far. The Pb atom off-centering can be well explained by the stereo-active $6s^2$ lone pairs, which are crystallographically more hidden in 3D perovskites. But in 2D perovskites with elongated bond lengths, as in the case of $(EA)_2(MHy)_2Pb_3Br_{10}$ and

$(EA)_2(EA)_2Pb_3Br_{10}$ (see below), the lone pairs are spatially expressed. They can distort the octahedral coordination geometry as the Pb atoms move off-centered dynamically. The stereochemical activity can be shown by the large bond angle variance and distortion index.

$$D = \frac{1}{6}\sum_i^6 \frac{|l_i - l_{av}|}{l_{av}} \quad (1)$$

$$\sigma^2 = \sum_{i=1}^{12} (\theta_i - 90)^2/11 \quad (2)$$

To accommodate the large A-site cations, the perovskite cages need to be expanded with elongated Pb-Br bond distances. As shown in Figure 2, the average Pb-Br bond length increases with larger A-site cation. The Pb-Br bond lengths can be further categorized into the equatorial bond length perpendicular to the stacking direction or the axial bond length parallel to the stacking axis. As shown in Table S7, $(BA)_2(MHy)_2Pb_3Br_{10}$ and $(BA)_2(EA)_2Pb_3Br_{10}$ have longer Pb-Br bond lengths than $(BA)_2(MA)_2Pb_3Br_{10}$ and $(BA)_2(Cs)_2Pb_3Br_{10}$, except for the external axial bond length. $(BA)_2(Cs)_2Pb_3Br_{10}$ exhibited the most uniform Pb-Br bond lengths, where the equatorial and axial bond lengths are similar. For the compounds incorporating an organic cation on the A-site, the internal axial Pb-Br bond length is longer than the external axial and equatorial Pb-Br bond lengths. It was recently reported that the compressive strain between the layers can balance the expansion of the perovskite cage and reduce the overall strain in the structure.[24-26] For $(BA)_2(MHy)_2Pb_3Br_{10}$, the (internal) axial and equatorial Pb-Br bond lengths are both elongated, whereas for $(BA)_2(EA)_2Pb_3Br_{10}$, the axial bond length is elongated more than the equatorial one. As shown in Figure 1d, the longest Pb-Br bond length in $(BA)_2(EA)_2Pb_3Br_{10}$ is 3.3 Å, which is much longer than the normal Pb-Br bond length (~3.0 Å). A similar phenomenon was observed in $(EA)_2(EA)_2Pb_3Br_{10}$, where the axial Pb-Br bond length was much longer than the equatorial one. The Pb-Br-Pb angle is also known to significantly influence the properties of 2D perovskites. The angles can also be categorized into axial and equatorial angles using the same criteria as the bond

length. $(BA)_2(Cs)_2Pb_3Br_{10}$ has the smallest equatorial and average Pb-Br-Pb angles because the size of $Cs^+$ is at the lower limit of the tolerance factor; therefore, the octahedra are tilted to accommodate the small A-site cation. $(BA)_2(MHy)_2Pb_3Br_{10}$ has larger equatorial Pb-Br-Pb angles than the other three compounds, but the average Pb-Br-Pb angles are quite similar to those of $(BA)_2(EA)_2Pb_3Br_{10}$ and $(BA)_2(MA)_2Pb_3Br_{10}$ (Table S8).

**n = 2 phases**

The new structure $(BA)_2(DMA)Pb_2Br_7$ adopts the same $Cmc2_1$ space group as previously reported in $(BA)_2(Cs)Pb_2Br_7$,[35] $(BA)_2(MA)Pb_2Br_7$,[32] and $(BA)_2(FA)Pb_2Br_7$[34] (Table 2), but its structure is slightly different. From the side view, $(BA)_2(DMA)Pb_2Br_7$ octahedra are clearly tilted out-of-plane (Figure 3a), but for $(BA)_2(MA)Pb_2Br_7$, the octahedra do not tilt out-of-plane (Figure 3b). From the top view (Figure 3c), the $(BA)_2(DMA)Pb_2Br_7$ octahedra are barely tilted in-plane, but for $(BA)_2(MA)Pb_2Br_7$, they are heavily tilted in-plane. For $(BA)_2(DMA)Pb_2Br_7$, there is a glide plane crossing the A-site cation, but for $(BA)_2(MA)Pb_2Br_7$, there is a mirror plane.

We also calculated the average Pb-Br bond length to evaluate cage expansion (Table S9, Figure S3). Both the equatorial and axial Pb-Br bond lengths increase with the size of the A-site cation, but for $(BA)_2(DMA)Pb_2Br_7$, there is a large increase in the average axial bond length because of the extra-long axial Pb-Br bond, as shown in Figure 3d-g. The average Pb-Br-Pb angles also increased with larger A-site cations (Table S9), similar to the 3D case of $CsPbBr_3$, $MAPbBr_3$, and $FAPbBr_3$. There are mainly two ways to accommodate the large A-site cations: the first is to elongate the Pb-Br bond length and the second is to straighten the equatorial Pb-Br-Pb angle. As shown in Table S9, the axial Pb-Br-Pb angles are close to 180°, while the equatorial angles increase as the size of the A-site cation increases. Since the angle cannot be larger than 180°, above a certain threshold, the bonds are elongated to accommodate the large A-site cation.

**DSC and phase transitions**

To assess the possibility of structural changes in the compounds with temperature, we measured the differential scanning calorimetry (DSC) for the compounds in the -80-150 ℃(193-423 K) range (Figure S4). The $(BA)_2(DMA)Pb_2Br_7$ compound shows a phase transition at approximately -36 ℃ (237 K), while the $(BA)_2(FA)Pb_2Br_7$, $(BA)_2(MHy)_2Pb_3Br_{10}$, and $(BA)_2(EA)_2Pb_3Br_{10}$ compounds do not exhibit phase transitions below room temperature. $(BA)_2(FA)Pb_2Br_7$ and $(BA)_2(EA)_2Pb_3Br_{10}$ compounds exhibited one phase transition above room temperature at 49 °C (322 K) and 108 °C (381 K), respectively. $(BA)_2(MHy)_2Pb_3Br_{10}$ has two phase transitions above room temperature: 98 °C (371 K) and 142 °C (415 K). $(BA)_2(Cs)Pb_2Br_7$ shows a broad peak around 100 °C (373 K), which corresponds to an isomorphic phase transition according to the literature.[35] At high temperatures (139 °C / 412 K), there is another small peak that corresponds to a second-order phase transition.[35] All compounds showed little hysteresis during the cycles because the peak positions remained almost unchanged in the first and second cycles. The phase transitions in 2D perovskites are usually attributed to the order-disorder transition of the organic spacer.[40] Since all the compounds reported here use BA as the spacer, they still have significantly different phase transition temperatures, suggesting that the A-site cations can also influence the phase transition temperatures as occurs in 3D $AMX_3$ perovskites.[41] For the n = 2 phases, they adopt the noncentrosymmetric $Ccm2_1$ space group at room temperature. It has been reported that they go through a noncentrosymmetric to centrosymmetric phase transition above room temperature for $(BA)_2(Cs)Pb_2Br_7$, $(BA)_2(MA)Pb_2Br_7$, and $(BA)_2(FA)Pb_2Br_7$.[32, 34, 35] For $(BA)_2(DMA)Pb_2Br_7$, this transition likely occurs at a higher temperature than our measurement range, and the low-temperature (-36 ℃) phase transition may correspond to the change from orthorhombic to monoclinic space groups. The phase transitions of $(BA)_2(MHy)_2Pb_3Br_{10}$ occur at high temperatures,

which is consistent with the trend that its 3D analogue, $(MHy)PbBr_3$, exhibits a phase transition at a relatively high temperature (145 °C),[19] likely because of the large distortion of the structure caused by strong hydrogen bonding.

**Electronic Band Structures**

DFT was used to calculate the electronic band structures of $(BA)_2(MHy)_2Pb_3Br_{10}$ and $(BA)_2(EA)_2Pb_3Br_{10}$ and compare them with those of $(BA)_2(Cs)_2Pb_3Br_{10}$ and $(BA)_2(MA)_2Pb_3Br_{10}$ based on the published structures (Figure 4). All n = 3 compounds are direct bandgap semiconductors, but they exhibit a sizable impact of the lattice distortion, including a Rashba splitting around the Γ (Y) or Y/2 points. The most striking example is $(BA)_2(MHy)_2Pb_3Br_{10}$, where k-dependent band splitting can be clearly observed at the Y/2 point. Notably, despite exhibiting the same space group (*Cc*), $(BA)_2(MHy)_2Pb_3Br_{10}$ and $(BA)_2(EA)_2Pb_3Br_{10}$ have different in-plane cell shapes, which explains why the location of the bandgap occurs at different high-symmetry points in the reciprocal space. The Rashba splitting originates from the noncentrosymmetric space groups along with sizable spin-orbit coupling, a direct consequence of the heavy lead atom[42], and has also been predicted in other noncentrosymmetric 2D[43] and 3D perovskite phases[44]. This significant Rashba splitting most likely stems from the off-centering of Pb atoms in $(BA)_2(MHy)_2Pb_3Br_{10}$, which leads to a break of symmetry and the splitting of the bands. This is among the largest Rashba splitting reported, which provides a new design strategy to induce Rashba splitting.

The band structures of all n = 3 compounds exhibit a clear 2D nature, where the bands are dispersive in the layer direction but flat in the stacking direction (Figure 4). The calculated bandgaps for $(BA)_2(MA)_2Pb_3Br_{10}$, $(BA)_2(Cs)_2Pb_3Br_{10}$, $(BA)_2(MHy)_2Pb_3Br_{10}$, and $(BA)_2(EA)_2Pb_3Br_{10}$ (Table 4) matched the experimental trend (see below and Figure S5). When

the Pb-Br-Pb angles were similar, compounds with larger organic A-site cations exhibited higher bandgaps. As the size of the A-site cation increases, the Pb-Br bonds are elongated, and in turn, the overlap between Pb s- and Br p-orbitals in the valence band decreases.[25] This leads to a shift of the valence band toward lower energies, thus opening the bandgap. This stabilization of the valence band is accompanied by a reduction in the valence band dispersion and an increase in the in-plane effective masses (Table 4). $(BA)_2(Cs)_2Pb_3Br_{10}$ had an intermediate bandgap and the smallest A cation. The larger bandgap compared to $(BA)_2(MA)_2Pb_3Br_{10}$ can be traced back to the significantly large in-plane tilting of the octahedra[23]. Similar trends were observed for the n = 2 phases (Table 4, Figure S6). As the size of the A-site cation increased from Cs to MA and from FA to DMA, the band dispersion decreased, especially for the valence bands (Figure S6) leading to increased bandgaps (Table 4). Meanwhile, because of the more pronounced in-plane octahedral tilting in $(BA)_2(Cs)Pb_2Br_7$ and $(BA)_2(MA)Pb_2Br_7$, as compared to $(BA)_2(FA)Pb_2Br_7$ and $(BA)_2(DMA)Pb_2Br_7$, their computed bandgaps are slightly larger. This suggests that both the Pb – Br–Pb and Pb-Br bond lengths can influence the bandgap of 2D perovskites. Notably, among the compounds in Table 4, the effective mass for holes is significantly larger in $(BA)_2(DMA)Pb_2Br_7$ which has the longest Pb-Br bond length and smallest band dispersion among the n = 2 phases.

**Optical Properties**

Absorption spectra were measured by diffuse reflectance of the grinded single crystals and converted to absorption by the Kubelka−Munk equation (Figure S7) and their Tauc plots are shown in Figure 5a,b.[45] In the absorption spectra (Figure 5a,b), there is a high-energy absorption edge and a low-energy exciton peak. In the case of $(BA)_2(MA)_2Pb_3Br_{10}$ (Figure S7a), a low-energy tail is observed that may originate from the high layer numbers. Even though we used the ratio of reagents as reported in the literature,[33] that report used a slow cooling method at a rate of 0.5 °C/day.

This slow cooling rate cannot be achieved with our furnace; therefore, we used a direct cooling method instead (the hot plate was turned off and the solution was cooled to room temperature after a clear solution was obtained). This procedure may cause the higher layer number or 3D impurities to be present in small amounts (below the detection limit of PXRD), however, the low-energy tail is not observable in the Tauc plot, as shown in Figure 5a. The position of the absorption edge matches that reported in the literature, so the impurity does not influence the extraction of the correct bandgap.[33] The bandgaps have been extracted either from the high-energy absorption edge or the low-energy slope as described previously.[32, 46] In either case, the bandgaps follow the trend $E_{g,\,EA} > \approx E_{g,MHy} > E_{g,MA}$ for n = 3 phases and $E_{g,\,DMA} > E_{g,\,FA} > \approx E_{g,\,MA} > \approx E_{g,Cs}$ for the n = 2 phases. It is worth pointing out that the change in the bandgaps (0.1- 0.2 eV) for the bromide system is larger than that in the iodide system $(BA)_2(A)Pb_2I_7$ (0.06 eV),[25] showing the power of tuning the optical properties by changing the A-site cations.

Generally, 2D perovskites with larger A-site cations exhibit larger bandgaps, except for $(BA)_2(Cs)_2Pb_3Br_{10}$. This is because they have the smallest Pb-Br-Pb angle, which reduces the overlap of the Pb s- and Br p-orbitals and increases the bandgap.[7] The larger bandgaps of $(BA)_2(MHy)_2Pb_3Br_{10}$ and $(BA)_2(EA)_2Pb_3Br_{10}$ compared to $(BA)_2(MA)_2Pb_3Br_{10}$ can be rationalized based on two independent structural features. First, although all three compounds have similar Pb-Br-Pb angles, $(BA)_2(MHy)_2Pb_3Br_{10}$ and $(BA)_2(EA)_2Pb_3Br_{10}$ have longer Pb-Br bonds, which can also reduce orbital overlap and increase the bandgap.[25] Second, $(BA)_2(MHy)_2Pb_3Br_{10}$ and $(BA)_2(EA)_2Pb_3Br_{10}$ also have a larger distortion index, which is reported to increase the bandgap.[47] For the n = 2 phase, both the Pb-Br-Pb bond angle (primarily the equatorial one) and the Pb-Br bond length increase with the increase in the size of the A-site cation. In $(BA)_2(Cs)Pb_2Br_7$, $(BA)_2(MA)Pb_2Br_7$, and $(BA)_2(FA)Pb_2Br_7$, these two factors compensate for

each other; therefore, they exhibit similar bandgaps. Considering the 2D color map reported in the literature,[25] the internal axial Pb-Br bond length has been shown to have a larger influence on the bandgap than the equatorial one. The $(BA)_2(DMA)Pb_2Br_7$ compound has an extra-long internal axial Pb-Br bond (Table S9), which is consistent with the fact that it has the highest bandgap among the n = 2 series. Collectively, these results suggest that both the Pb-Br-Pb angle and Pb-Br can influence the bandgap and may sometimes compensate each other until one of the factors dominates.

The PL spectra of some of the compounds are shown in Figure 5c. The PL spectra of $(BA)_2(EA)_2Pb_3Br_{10}$ and $(BA)_2(DMA)Pb_2Br_7$ were relatively broad. The other three compounds exhibit a narrow PL peak and a broad shoulder, and their origins will be discussed below. As seen in the PL decay curves (Figure 5d), the compounds exhibit a fast decay for the first nanosecond, followed by a slow decay. Therefore, the curves are fitted to a two-exponential decay, $\tau = a_1 \times e^{\tau_1} + a_2 \times e^{\tau_2} + b$, where $\tau_1$ and $\tau_2$ correspond to the lifetimes of the fast and slow components, respectively. The ratio of the number of photons emitted in each decay can be calculated using $Ph_x = (a_x \times \tau_x)/(a_1 \times \tau_1 + a_2 \times \tau_2)$, (x = 1, 2). Then, the average lifetime can be defined by $\tau_{avg} = Ph_1 \times \tau_1 + Ph_2 \times \tau_2$, and the fitted values produced in this manner are listed in Table 5. The PL lifetimes follow the trend $\tau_{ave,\,Cs} > \tau_{ave,\,FA} > \tau_{ave,\,EA} > \tau_{ave,\,DMA} > \tau_{ave,\,MHy.}$ Generally, the PL lifetimes of the 2D perovskites with larger A-site cations are shorter than those with smaller A cations. This is consistent with previous reports that 2D perovskites with larger A-site cations show shorter PL lifetimes[25] because they have softer and more anharmonic lattices (see below), which makes the compounds subject to defect states that induce exciton trapping.

To explore the origin of the broad (shoulder) PL, we chose to measure the temperature-dependent PL of $(BA)_2(EA)_2Pb_3Br_{10}$ for the reported compounds (Figure 6). As the temperature decreased,

the broad peak evolved into a narrow peak and a shoulder at longer wavelengths. At 78 K, the main peak (free exciton peak) became much narrower, and the shoulder almost completely disappeared. Meanwhile, a new broad peak appeared at approximately 610 nm, which was red-shifted with respect to the shoulder peak. This temperature-activated effect was also observed by other researchers, who attributed the broad emission to trap states.[48-51] The PL lifetimes were fitted as discussed above. The fitting parameters are summarized in Table S10 and the average lifetimes are shown in Figure 6b. The fast decay can be attributed to the radiative excitonic decay and the slower one is believed to be related to trapping. The PL lifetime first increased with decreasing temperature, reached its maximum at 135 K, and then decreased again at 78 K when the shoulder peak disappeared. To confirm this, we measured the power-dependent PL at room temperature (Figure 6c). The PL intensity saturates at high power density. For an excitonic emission, we would expect it to follow a linear relationship. The saturation of PL at high power suggests that part of the emission (the shoulder) originates from the trap states, since we assume there is only a limited number of traps.[41]

We also explored the lattice softness and phonon modes using low-frequency Raman spectroscopy. The room temperature spectra are shown in Figure 7a. They consist of a broad, diffuse central peak around 0 $cm^{-1}$, as well as distinct peaks, with the main peaks shift from 47 to 73 $cm^{-1}$, which can be attributed to the bending modes of the octahedra.[52] The frequency of the main peak shifts to a lower wavenumber as the size of the A-site cation increases, which corresponds to lower frequency phonons because of the weaker, longer-length Pb-Br bond. The temperature-dependent Raman spectra for $(BA)_2(EA)_2Pb_3Br_{10}$ appear similar across the measured temperature range (Figure 7b), which is consistent with the DSC result that there is no phase transition in the temperature range. The temperature-dependent Raman spectra of the other compounds are shown in Figure S8. For

$(BA)_2(Cs)Pb_2Br_7$ and $(BA)_2(FA)Pb_2Br_7$, the peaks become slightly more distinct at low temperatures, while for $(BA)_2(DMA)Pb_2Br_7$, they are still diffuse. This suggests that the perovskite lattice with larger A-site cations is even softer and more anharmonic, possibly making it easier to interact with the charge carriers, resulting in a shorter PL lifetime. It was shown that lattice softness can influence the trapping of carriers by shallow traps and, in turn, the quantum yield.[53] Although the dynamic lattice is responsible for many favorable physical properties of halide perovskites, once passing a certain range (e.g., with the large A cations discussed here), the softer lattice may be detrimental to certain properties.

## Conclusions

Large A-site cations in 2D perovskites can lead not only to cage expansion but also to large octahedral distortion and Pb off-centering. The *A-B-A* distorted and undistorted stacking pattern explains why only the n = 3 phase can be stabilized for MHy and EA. The Pb off-centering in $(BA)_2(MHy)_2Pb_3Br_{10}$ causes a large Rashba splitting in the calculated electronic band structure. Both the Pb-Br bond length and the Pb-Br-Pb angle can influence the optical properties of 2D perovskites. For similar tilting of the octahedra, as the size of the A-site cation increases, the band dispersion becomes smaller, resulting in a larger carrier effective mass and larger bandgap. The Pb off-centering in $(BA)_2(MHy)_2Pb_3Br_{10}$ leads to one of the largest Rashba splitting in the literature. The PL spectra of EA exhibited a shoulder at room temperature and an additional broad peak at low temperatures. Low-frequency Raman spectra suggest that the lattice also becomes softer and more anharmonic with the increasing size of the A-site cation. The oversoft lattice may be subject to trap formation, which is responsible for the shorter PL lifetime for structures with larger A cations. These new structures expand the platform of 2D perovskites to study the structure–property relationships with large A-site cations.

## ASSOCIATED CONTENT

## Supporting Information

Additional experimental details, crystallographic details, DSC curves, additional DFT calculation results, and temperature-dependent Raman spectra.

X-ray crystallographic data of $(BA)_2(MHy)_2Pb_3Br_{10}$.

X-ray crystallographic data of $(BA)_2(EA)_2Pb_3Br_{10}$.

X-ray crystallographic data of $(BA)_2(DMA)Pb_2Br_7$.

## Author information

### Corresponding Author

*m-kanatzidis@northwestern.edu

### Notes

The authors declare no competing financial interest.

## Acknowledgments

At Northwestern University, this work is mainly supported by the Department of Energy, Office of Science, Basic Energy Sciences, under Grant No. SC0012541 (synthesis, structure, and characterization of physical properties) This work was performed, in part, at the Center for Nanoscale Materials, a U.S. Department of Energy Office of Science User Facility, and supported by the U.S. Department of Energy, Office of Science, under Contract No. DE-AC02-06CH11357. A. B. acknowledges support from Region Bretagne through the PERFOTON project. J. E. acknowledges financial support from the Institut Universitaire de France. B.T., C.K., and J.E. acknowledge funding from the European Union's Horizon 2020 research and innovation program under grant agreement No. 861985. The work at Yale was supported by the Yale University Lab Setup Fund. This work used the IMSERC facility at Northwestern University, which has received

support from the Soft and Hybrid Nanotechnology Experimental (SHyNE) Resource (NSF ECCS-2025633), and Northwestern University.

## References

1. Hassan, Y.; Park, J. H.; Crawford, M. L.; Sadhanala, A.; Lee, J.; Sadighian, J. C.; Mosconi, E.; Shivanna, R.; Radicchi, E.; Jeong, M.; Yang, C.; Choi, H.; Park, S. H.; Song, M. H.; De Angelis, F.; Wong, C. Y.; Friend, R. H.; Lee, B. R.; Snaith, H. J., Ligand-engineered bandgap stability in mixed-halide perovskite LEDs. *Nature* **2021,** *591* (7848), 72-77.
2. Yoo, J. J.; Seo, G.; Chua, M. R.; Park, T. G.; Lu, Y.; Rotermund, F.; Kim, Y.-K.; Moon, C. S.; Jeon, N. J.; Correa-Baena, J.-P.; Bulović, V.; Shin, S. S.; Bawendi, M. G.; Seo, J., Efficient perovskite solar cells via improved carrier management. *Nature* **2021,** *590* (7847), 587-593.
3. Qin, C.; Sandanayaka, A. S. D.; Zhao, C.; Matsushima, T.; Zhang, D.; Fujihara, T.; Adachi, C., Stable room-temperature continuous-wave lasing in quasi-2D perovskite films. *Nature* **2020,** *585* (7823), 53-57.
4. Dong, Q.; Fang, Y.; Shao, Y.; Mulligan, P.; Qiu, J.; Cao, L.; Huang, J., Electron-hole diffusion lengths >175 μm in solution-grown $CH_3NH_3PbI_3$ single crystals. *Science* **2015,** *347* (6225), 967-970.
5. Xing, G.; Mathews, N.; Sun, S.; Lim, S. S.; Lam, Y. M.; Grätzel, M.; Mhaisalkar, S.; Sum, T. C., Long-Range Balanced Electron- and Hole-Transport Lengths in Organic-Inorganic $CH_3NH_3PbI_3$. *Science* **2013,** *342* (6156), 344-347.
6. Shi, D.; Adinolfi, V.; Comin, R.; Yuan, M.; Alarousu, E.; Buin, A.; Chen, Y.; Hoogland, S.; Rothenberger, A.; Katsiev, K.; Losovyj, Y.; Zhang, X.; Dowben, P. A.; Mohammed, O. F.; Sargent, E. H.; Bakr, O. M., Low trap-state density and long carrier diffusion in organolead trihalide perovskite single crystals. *Science* **2015,** *347* (6221), 519-522.
7. Stoumpos, C. C.; Kanatzidis, M. G., The Renaissance of Halide Perovskites and Their Evolution as Emerging Semiconductors. *Acc. Chem. Res.* **2015,** *48* (10), 2791-2802.
8. Stoumpos, C. C.; Kanatzidis, M. G., Halide Perovskites: Poor Man's High-Performance Semiconductors. *Adv. Mater.* **2016,** *28* (28), 5778-5793.
9. Kieslich, G.; Sun, S.; Cheetham, A. K., Solid-state principles applied to organic–inorganic perovskites: new tricks for an old dog. *Chem. Sci.* **2014,** *5* (12), 4712-4715.
10. Kieslich, G.; Sun, S.; Cheetham, A. K., An extended Tolerance Factor approach for organic–inorganic perovskites. *Chem. Sci.* **2015,** *6* (6), 3430-3433.
11. Saliba, M.; Matsui, T.; Domanski, K.; Seo, J.-Y.; Ummadisingu, A.; Zakeeruddin, S. M.; Correa-Baena, J.-P.; Tress, W. R.; Abate, A.; Hagfeldt, A.; Grätzel, M., Incorporation of rubidium cations into perovskite solar cells improves photovoltaic performance. *Science* **2016,** *354* (6309), 206-209.
12. Correa-Baena, J.-P.; Luo, Y.; Brenner, T. M.; Snaider, J.; Sun, S.; Li, X.; Jensen, M. A.; Hartono, N. T. P.; Nienhaus, L.; Wieghold, S.; Poindexter, J. R.; Wang, S.; Meng, Y. S.; Wang, T.; Lai, B.; Holt, M. V.; Cai, Z.; Bawendi, M. G.; Huang, L.; Buonassisi, T.; Fenning, D. P., Homogenized halides and alkali cation segregation in alloyed organic-inorganic perovskites. *Science* **2019,** *363* (6427), 627-631.
13. Gao, L.; Li, X.; Liu, Y.; Fang, J.; Huang, S.; Spanopoulos, I.; Li, X.; Wang, Y.; Chen, L.; Yang, G.; Kanatzidis, M. G., Incorporated Guanidinium Expands the CH3NH3PbI3 Lattice and Enhances Photovoltaic Performance. *ACS Appl. Mater. Interfaces* **2020,** *12* (39), 43885-43891.
14. Anelli, C.; Chierotti, M. R.; Bordignon, S.; Quadrelli, P.; Marongiu, D.; Bongiovanni, G.; Malavasi, L., Investigation of Dimethylammonium Solubility in MAPbBr3 Hybrid Perovskite: Synthesis, Crystal Structure, and Optical Properties. *Inorg. Chem.* **2019,** *58* (1), 944-949.
15. Kubicki, D. J.; Prochowicz, D.; Hofstetter, A.; Saski, M.; Yadav, P.; Bi, D.; Pellet, N.; Lewiński, J.; Zakeeruddin, S. M.; Grätzel, M.; Emsley, L., Formation of Stable Mixed Guanidinium–Methylammonium Phases with Exceptionally Long Carrier Lifetimes for High-Efficiency Lead Iodide-Based Perovskite Photovoltaics. *J. Am. Chem. Soc.* **2018,** *140* (9), 3345-3351.

16. Huang, S.; Huang, P.; Wang, L.; Han, J.; Chen, Y.; Zhong, H., Halogenated-Methylammonium Based 3D Halide Perovskites. *Adv. Mater.* **2019,** *31* (42), 1903830.
17. Zhang, H.-Y.; Chen, X.-G.; Zhang, Z.-X.; Song, X.-J.; Zhang, T.; Pan, Q.; Zhang, Y.; Xiong, R.-G., Methylphosphonium Tin Bromide: A 3D Perovskite Molecular Ferroelectric Semiconductor. *Adv. Mater.* **2020,** *32* (47), 2005213.
18. Mączka, M.; Gagor, A.; Zaręba, J. K.; Stefanska, D.; Drozd, M.; Balciunas, S.; Šimėnas, M.; Banys, J.; Sieradzki, A., Three-Dimensional Perovskite Methylhydrazinium Lead Chloride with Two Polar Phases and Unusual Second-Harmonic Generation Bistability above Room Temperature. *Chemistry of Materials* **2020,** *32* (9), 4072-4082.
19. Mączka, M. a.; Ptak, M.; Gągor, A.; Stefańska, D.; Zaręba, J. K.; Sieradzki, A., Methylhydrazinium Lead Bromide: Noncentrosymmetric Three-Dimensional Perovskite with Exceptionally Large Framework Distortion and Green Photoluminescence. *Chem. Mater.* **2020,** *32* (4), 1667-1673.
20. Mączka, M.; Ptak, M.; Gągor, A.; Stefańska, D.; Sieradzki, A., Layered Lead Iodide of [Methylhydrazinium]2PbI4 with a Reduced Band Gap: Thermochromic Luminescence and Switchable Dielectric Properties Triggered by Structural Phase Transitions. *Chem. Mater.* **2019,** *31* (20), 8563-8575.
21. Mączka, M.; Zaręba, J. K.; Gągor, A.; Stefańska, D.; Ptak, M.; Roleder, K.; Kajewski, D.; Soszyński, A.; Fedoruk, K.; Sieradzki, A., [Methylhydrazinium]2PbBr4, a Ferroelectric Hybrid Organic–Inorganic Perovskite with Multiple Nonlinear Optical Outputs. *Chem. Mater.* **2021,** *33* (7), 2331-2342.
22. Stoumpos, C. C.; Mao, L.; Malliakas, C. D.; Kanatzidis, M. G., Structure–Band Gap Relationships in Hexagonal Polytypes and Low-Dimensional Structures of Hybrid Tin Iodide Perovskites. *Inorg. Chem.* **2017,** *56* (1), 56-73.
23. Mao, L.; Wu, Y.; Stoumpos, C. C.; Traore, B.; Katan, C.; Even, J.; Wasielewski, M. R.; Kanatzidis, M. G., Tunable White-Light Emission in Single-Cation-Templated Three-Layered 2D Perovskites $(CH_3CH_2NH_3)_4Pb_3Br_{10-x}Cl_x$. *J. Am. Chem. Soc.* **2017,** *139* (34), 11956-11963.
24. Fu, Y.; Hautzinger, M. P.; Luo, Z.; Wang, F.; Pan, D.; Aristov, M. M.; Guzei, I. A.; Pan, A.; Zhu, X.; Jin, S., Incorporating Large A Cations into Lead Iodide Perovskite Cages: Relaxed Goldschmidt Tolerance Factor and Impact on Exciton–Phonon Interaction. *ACS Cent. Sci.* **2019,** *5* (8), 1377-1386.
25. Li, X.; Fu, Y.; Pedesseau, L.; Guo, P.; Cuthriell, S.; Hadar, I.; Even, J.; Katan, C.; Stoumpos, C. C.; Schaller, R. D.; Harel, E.; Kanatzidis, M. G., Negative Pressure Engineering with Large Cage Cations in 2D Halide Perovskites Causes Lattice Softening. *J. Am. Chem. Soc.* **2020,** *142* (26), 11486-11496.
26. Fu, Y.; Jiang, X.; Li, X.; Traore, B.; Spanopoulos, I.; Katan, C.; Even, J.; Kanatzidis, M. G.; Harel, E., Cation Engineering in Two-Dimensional Ruddlesden-Popper Lead Iodide Perovskites with Mixed Large A-Site Cations in the Cages. *J. Am. Chem. Soc.* **2020,** *142* (8), 4008-4021.
27. Ji, C.; Wang, S.; Wang, Y.; Chen, H.; Li, L.; Sun, Z.; Sui, Y.; Wang, S.; Luo, J., 2D Hybrid Perovskite Ferroelectric Enables Highly Sensitive X-Ray Detection with Low Driving Voltage. *Adv. Funct. Mater.* **2020,** *30* (5), 1905529.
28. Han, S.; Liu, X.; Liu, Y.; Xu, Z.; Li, Y.; Hong, M.; Luo, J.; Sun, Z., High-Temperature Antiferroelectric of Lead Iodide Hybrid Perovskites. *J. Am. Chem. Soc.* **2019,** *141* (32), 12470-12474.
29. Liu, Y.; Han, S.; Wang, J.; Ma, Y.; Guo, W.; Huang, X.-Y.; Luo, J.-H.; Hong, M.; Sun, Z., Spacer Cation Alloying of a Homoconformational Carboxylate trans Isomer to Boost in-Plane Ferroelectricity in a 2D Hybrid Perovskite. *J. Am. Chem. Soc.* **2021,** *143* (4), 2130-2137.
30. Mao, L.; Guo, P.; Kepenekian, M.; Hadar, I.; Katan, C.; Even, J.; Schaller, R. D.; Stoumpos, C. C.; Kanatzidis, M. G., Structural Diversity in White-Light-Emitting Hybrid Lead Bromide Perovskites. *J. Am. Chem. Soc.* **2018,** *140* (40), 13078-13088.
31. Umeyama, D.; Leppert, L.; Connor, B.; Manumpil, M. A.; Neaton, J.; Karunadasa, H., Expanded Analogs of Three-Dimensional Lead-Halide Hybrid Perovskites. *Angew. Chem., Int. Ed.* **2020,** *59* (43), 19087-19094.

32. Li, L.; Liu, X.; Li, Y.; Xu, Z.; Wu, Z.; Han, S.; Tao, K.; Hong, M.; Luo, J.; Sun, Z., Two-Dimensional Hybrid Perovskite-Type Ferroelectric for Highly Polarization-Sensitive Shortwave Photodetection. *J. Am. Chem. Soc.* **2019,** *141* (6), 2623-2629.
33. Li, L.; Sun, Z.; Wang, P.; Hu, W.; Wang, S.; Ji, C.; Hong, M.; Luo, J., Tailored Engineering of an Unusual $(C_4H_9NH_3)_2(CH_3NH_3)_2Pb_3Br_{10}$ Two-Dimensional Multilayered Perovskite Ferroelectric for a High-Performance Photodetector. *Angew. Chem., Int. Ed.* **2017,** *56* (40), 12150-12154.
34. Li, L.; Shang, X.; Wang, S.; Dong, N.; Ji, C.; Chen, X.; Zhao, S.; Wang, J.; Sun, Z.; Hong, M.; Luo, J., Bilayered Hybrid Perovskite Ferroelectric with Giant Two-Photon Absorption. *J. Am. Chem. Soc.* **2018,** *140* (22), 6806-6809.
35. Wu, Z.; Ji, C.; Li, L.; Kong, J.; Sun, Z.; Zhao, S.; Wang, S.; Hong, M.; Luo, J., Alloying n-Butylamine into CsPbBr3 To Give a Two-Dimensional Bilayered Perovskite Ferroelectric Material. *Angew. Chem., Int. Ed.* **2018,** *57* (27), 8140-8143.
36. Li, X.; Hoffman, J.; Ke, W.; Chen, M.; Tsai, H.; Nie, W.; Mohite, A. D.; Kepenekian, M.; Katan, C.; Even, J.; Wasielewski, M. R.; Stoumpos, C. C.; Kanatzidis, M. G., Two-Dimensional Halide Perovskites Incorporating Straight Chain Symmetric Diammonium Ions, $(NH_3C_mH_{2m}NH_3)(CH_3NH_3)_{n-1}Pb_nI_{3n+1}$ (m = 4–9; n = 1–4). *J. Am. Chem. Soc.* **2018,** *140* (38), 12226-12238.
37. Li, X.; Ke, W.; Traoré, B.; Guo, P.; Hadar, I.; Kepenekian, M.; Even, J.; Katan, C.; Stoumpos, C. C.; Schaller, R. D.; Kanatzidis, M. G., Two-Dimensional Dion–Jacobson Hybrid Lead Iodide Perovskites with Aromatic Diammonium Cations. *J. Am. Chem. Soc.* **2019,** *141* (32), 12880-12890.
38. Soe, C. M. M.; Stoumpos, C. C.; Kepenekian, M.; Traoré, B.; Tsai, H.; Nie, W.; Wang, B.; Katan, C.; Seshadri, R.; Mohite, A. D.; Even, J.; Marks, T. J.; Kanatzidis, M. G., New Type of 2D Perovskites with Alternating Cations in the Interlayer Space, $(C(NH_2)_3)(CH_3NH_3)_nPb_nI_{3n+1}$: Structure, Properties, and Photovoltaic Performance. *J. Am. Chem. Soc.* **2017,** *139* (45), 16297-16309.
39. Momma, K.; Izumi, F., VESTA 3 for three-dimensional visualization of crystal, volumetric and morphology data. *J. Appl. Crystallogr.* **2011,** *44* (6), 1272-1276.
40. Barman, S.; Venkataraman, N. V.; Vasudevan, S.; Seshadri, R., Phase Transitions in the Anchored Organic Bilayers of Long-Chain Alkylammonium Lead Iodides $(C_nH_{2n+1}NH_3)_2PbI_4$; n = 12, 16, 18. *J. Phys. Chem. B* **2003,** *107* (8), 1875-1883.
41. Chen, C.; Hu, X.; Lu, W.; Chang, S.; Shi, L.; Li, L.; Zhong, H.; Han, J.-B., Elucidating the phase transitions and temperature-dependent photoluminescence of MAPbBr3 single crystal. *Journal of Physics D: Applied Physics* **2018,** *51* (4), 045105.
42. Even, J.; Pedesseau, L.; Dupertuis, M. A.; Jancu, J. M.; Katan, C., Electronic model for self-assembled hybrid organic/perovskite semiconductors: Reverse band edge electronic states ordering and spin-orbit coupling. *Phys. Rev. B* **2012,** *86* (20), 205301.
43. Kepenekian, M.; Robles, R.; Katan, C.; Sapori, D.; Pedesseau, L.; Even, J., Rashba and Dresselhaus Effects in Hybrid Organic–Inorganic Perovskites: From Basics to Devices. *ACS Nano* **2015,** *9* (12), 11557-11567.
44. Even, J.; Pedesseau, L.; Jancu, J.-M.; Katan, C., DFT and k · p modelling of the phase transitions of lead and tin halide perovskites for photovoltaic cells. *physica status solidi (RRL) – Rapid Research Letters* **2014,** *8* (1), 31-35.
45. Gate, L. F., Comparison of the Photon Diffusion Model and Kubelka-Munk Equation with the Exact Solution of the Radiative Transport Equation. *Appl. Opt.* **1974,** *13* (2), 236-238.
46. Stoumpos, C. C.; Cao, D. H.; Clark, D. J.; Young, J.; Rondinelli, J. M.; Jang, J. I.; Hupp, J. T.; Kanatzidis, M. G., Ruddlesden–Popper Hybrid Lead Iodide Perovskite 2D Homologous Semiconductors. *Chem. Mater.* **2016,** *28* (8), 2852-2867.
47. Li, X.; He, Y.; Kepenekian, M.; Guo, P.; Ke, W.; Even, J.; Katan, C.; Stoumpos, C. C.; Schaller, R. D.; Kanatzidis, M. G., Three-dimensional Lead Iodide Perovskitoid Hybrids with High X-ray Photoresponse. *J. Am. Chem. Soc.* **2020,** *142* (14), 6625-6637.

48. Wu, X.; Trinh, M. T.; Niesner, D.; Zhu, H.; Norman, Z.; Owen, J. S.; Yaffe, O.; Kudisch, B. J.; Zhu, X. Y., Trap States in Lead Iodide Perovskites. *J. Am. Chem. Soc.* **2015,** *137* (5), 2089-2096.
49. Paritmongkol, W.; Powers, E. R.; Dahod, N. S.; Tisdale, W. A., Two Origins of Broadband Emission in Multilayered 2D Lead Iodide Perovskites. *J. Phys. Chem. Lett.* **2020**, 8565-8572.
50. Booker, E. P.; Thomas, T. H.; Quarti, C.; Stanton, M. R.; Dashwood, C. D.; Gillett, A. J.; Richter, J. M.; Pearson, A. J.; Davis, N. J. L. K.; Sirringhaus, H.; Price, M. B.; Greenham, N. C.; Beljonne, D.; Dutton, S. E.; Deschler, F., Formation of Long-Lived Color Centers for Broadband Visible Light Emission in Low-Dimensional Layered Perovskites. *J. Am. Chem. Soc.* **2017,** *139* (51), 18632-18639.
51. Stranks, S. D.; Burlakov, V. M.; Leijtens, T.; Ball, J. M.; Goriely, A.; Snaith, H. J., Recombination Kinetics in Organic-Inorganic Perovskites: Excitons, Free Charge, and Subgap States. *Phys. Rev. Appl.* **2014,** *2* (3), 034007.
52. Guo, P.; Xia, Y.; Gong, J.; Cao, D. H.; Li, X.; Li, X.; Zhang, Q.; Stoumpos, C. C.; Kirschner, M. S.; Wen, H.; Prakapenka, V. B.; Ketterson, J. B.; Martinson, A. B. F.; Xu, T.; Kanatzidis, M. G.; Chan, M. K. Y.; Schaller, R. D., Direct Observation of Bandgap Oscillations Induced by Optical Phonons in Hybrid Lead Iodide Perovskites. *Adv. Funct. Mater.* **2020**, 1907982.
53. Gong, X.; Voznyy, O.; Jain, A.; Liu, W.; Sabatini, R.; Piontkowski, Z.; Walters, G.; Bappi, G.; Nokhrin, S.; Bushuyev, O.; Yuan, M.; Comin, R.; McCamant, D.; Kelley, S. O.; Sargent, E. H., Electron–phonon interaction in efficient perovskite blue emitters. *Nat. Mater.* **2018,** *17* (6), 550-556.

Table 1. The Effective Radii of the Cations.[9, 20]

| Cation | Structural Formula | Effective Radius (pm) | Tolerance Factor |
|---|---|---|---|
| Cesium (Cs) | $Cs^+$ | 181 | 0.81 |
| Methylammonium (MA) | $CH_3NH_3^+$ | 217 | 0.89 |
| Formamidinium (FA) | $HC(NH_2)_2^+$ | 253 | 0.98 |
| Methylhydrazinium (MHy) | $CH_3NH_2NH_2^+$ | 264 | 1.01 |
| Dimethylammonium (DMA) | $CH_3NH_2CH_3^+$ | 272 | 1.02 |
| Ethylammonium (EA) | $CH_3CH_2NH_3^+$ | 274 | 1.03 |

Table 2. Crystal and Refinement Data for Three New Structures Reported Here.

| Compound | **$(BA)_2(MHy)_2Pb_3Br_{10}$** | **$(BA)_2(EA)_2Pb_3Br_{10}$** | **$(BA)_2(DMA)Pb_2Br_7$** |
|---|---|---|---|
| Crystal system | monoclinic | monoclinic | orthorhombic |
| Space group | *Cc* | *Cc* | $Ccm2_1$ |
| Unit cell dimensions | a = 51.406(10) Å<br>b = 5.9636(12) Å<br>c = 11.855(2) Å<br>β = 96.66(3)° | a = 50.952(10) Å<br>b = 8.4690(17) Å<br>c = 8.4547(17) Å<br>β = 90.026° | a = 39.637(8) Å<br>b = 8.3784(11) Å<br>c = 8.5023(14) Å |
| Volume | 3609.8(12) $Å^3$ | 3648.3(13) $Å^3$ | 2823.6(8) $Å^3$ |
| Z | 4 | 4 | 4 |
| Density (calculated) | 3.0601 $g/cm^3$ | 3.0242 $g/cm^3$ | 2.7478 $g/cm^3$ |
| Index ranges | -70<=h<=70<br>-8<=k<=8<br>-16<=l<=16 | -66<=h<=69<br>-11<=k<=11<br>-11<=l<=11 | -53<=h<=54<br>-11<=k<=11<br>-11<=l<=11 |
| Reflections collected | 29833 | 17182 | 13535 |
| Independent reflections | 6435 [$R_{int}$ = 0.1523] | 6313 [$R_{int}$ = 0.0594] | 2722 [$R_{int}$ = 0.0447] |
| Completeness to θ = 25° | 100% | 100% | 99% |
| Data / restraints / parameters | 6435 / 20 / 171 | 6313 / 20 / 171 | 2722 / 17 / 79 |
| Goodness-of-fit | 3.23 | 1.44 | 2.60 |
| Final R indices [I>2σ(I)] | $R_{obs}$ = 0.0784<br>$wR_{obs}$ = 0.0793 | $R_{obs}$ = 0.0489<br>$wR_{obs}$ = 0.0395 | $R_{obs}$ = 0.0511<br>$wR_{obs}$ = 0.0528 |
| R indices [all data] | $R_{all}$ = 0.0897,<br>$wR_{all}$ = 0.0798 | $R_{all}$ = 0.0744<br>$wR_{all}$ = 0.0416 | $R_{all}$ = 0.0755<br>$wR_{all}$ = 0.0543 |
| Largest diff. peak and hole | 2.61 and -3.73 $e·Å^{-3}$ | 1.34 and -1.11 $e·Å^{-3}$ | 1.97 and -1.80 $e·Å^{-3}$ |

Table 3. Comparison of the Distortion Index and Bond Angle Variance for the n = 3 Phases.

| | Distortion Index | | | | Bond Angle Variance | | | |
|---|---|---|---|---|---|---|---|---|
| | Cs | MA | MHy | EA | Cs | MA | MHy | EA |
| Layer 1 | 0.002 | 0.015 | 0.018 | 0.032 | 8.3 | 11.6 | 6.7 | 36.0 |
| Layer 2 | 0.001 | 0.008 | 0.024 | 0.016 | 0.4 | 5.4 | 274.0 | 21.2 |
| Layer 3 | 0.002 | 0.015 | 0.018 | 0.034 | 8.3 | 11.6 | 6.5 | 34.2 |
| Ave | 0.002 | 0.013 | 0.020 | 0.028 | 5.7 | 9.6 | 95.7 | 30.6 |

Table 4. Comparison of Calculated Bandgaps and Effective Masses as extracted at the extrema of the valence and conduction bands

| Compound | $m_h$ ($m_0$) | $m_e$ ($m_0$) | $\mu$ ($m_0$) | Eg (eV) |
|---|---|---|---|---|
| $(BA)_2(Cs)Pb_2Br_7$ | 0.22 | 0.22 | 0.11 | 1.38 |
| $(BA)_2(MA)Pb_2Br_7$ | 0.26 | 0.21 | 0.12 | 1.46 |
| $(BA)_2(FA)Pb_2Br_7$ | 0.26 | 0.22 | 0.12 | 1.33 |
| $(BA)_2(DMA)Pb_2Br_7$ | 0.45 | 0.19 | 0.13 | 1.40 |
| $(BA)_2(Cs)_2Pb_3Br_{10}$ | 0.22 | 0.2 | 0.10 | 1.17 |
| $(BA)_2(MA)_2Pb_3Br_{10}$ | 0.22 | 0.19 | 0.10 | 0.96 |
| $(BA)_2(MHy)_2Pb_3Br_{10}$ | 0.25 | 0.34 | 0.14 | 1.21 |
| $(BA)_2(EA)_2Pb_3Br_{10}$ | 0.28 | 0.23 | 0.13 | 1.38 |

Table 5. Summary of PL Lifetimes and Fitting Parameters.

| | $a_1$ | $\tau_1$ (ns) | $a_2$ | $\tau_2$ (ns) | $\tau_{ave}$ (ns) |
|---|---|---|---|---|---|
| $(BA)_2(Cs)Pb_2Br_7$ | 0.990 | 0.103 | 0.010 | 1.461 | 0.277 |
| $(BA)_2(FA)Pb_2Br_7$ | 0.992 | 0.106 | 0.008 | 1.399 | 0.236 |
| $(BA)_2(DMA)Pb_2Br_7$ | 0.992 | 0.110 | 0.008 | 0.793 | 0.149 |
| $(BA)_2(MHy)_2Pb_3Br_{10}$ | 0.996 | 0.099 | 0.004 | 0.954 | 0.127 |
| $(BA)_2(EA)_2Pb_3Br_{10}$ | 0.987 | 0.126 | 0.013 | 0.964 | 0.204 |

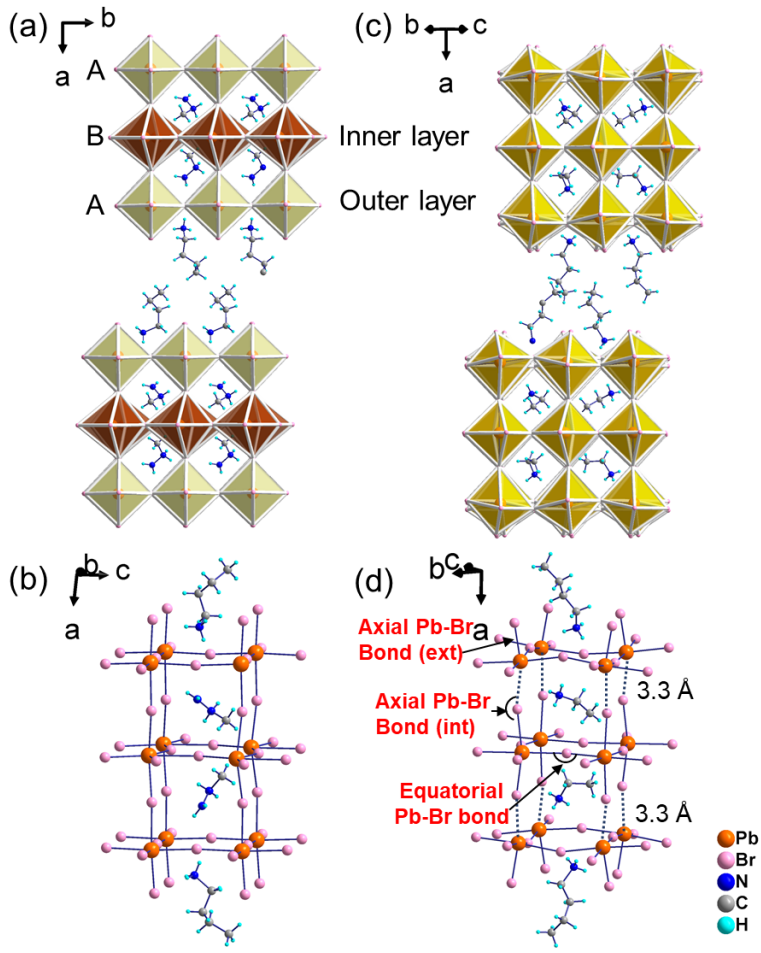


Figure 1. Views of crystal structures of (a),(b) $(BA)_2(MHy)_2Pb_3Br_{10}$ and (c),(d) $(BA)_2(EA)_2Pb_3Br_{10}$.

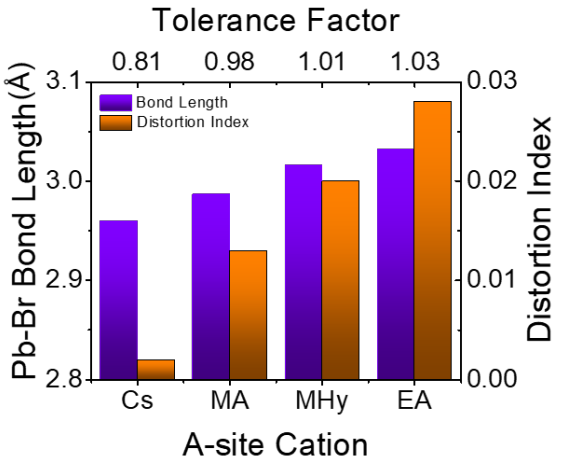


Figure 2. The relationships between the cation, tolerance factor, Pb-Br bond length and distortion index for n = 3 $(BA)_2(A)_2Pb_3Br_{10}$ phases.

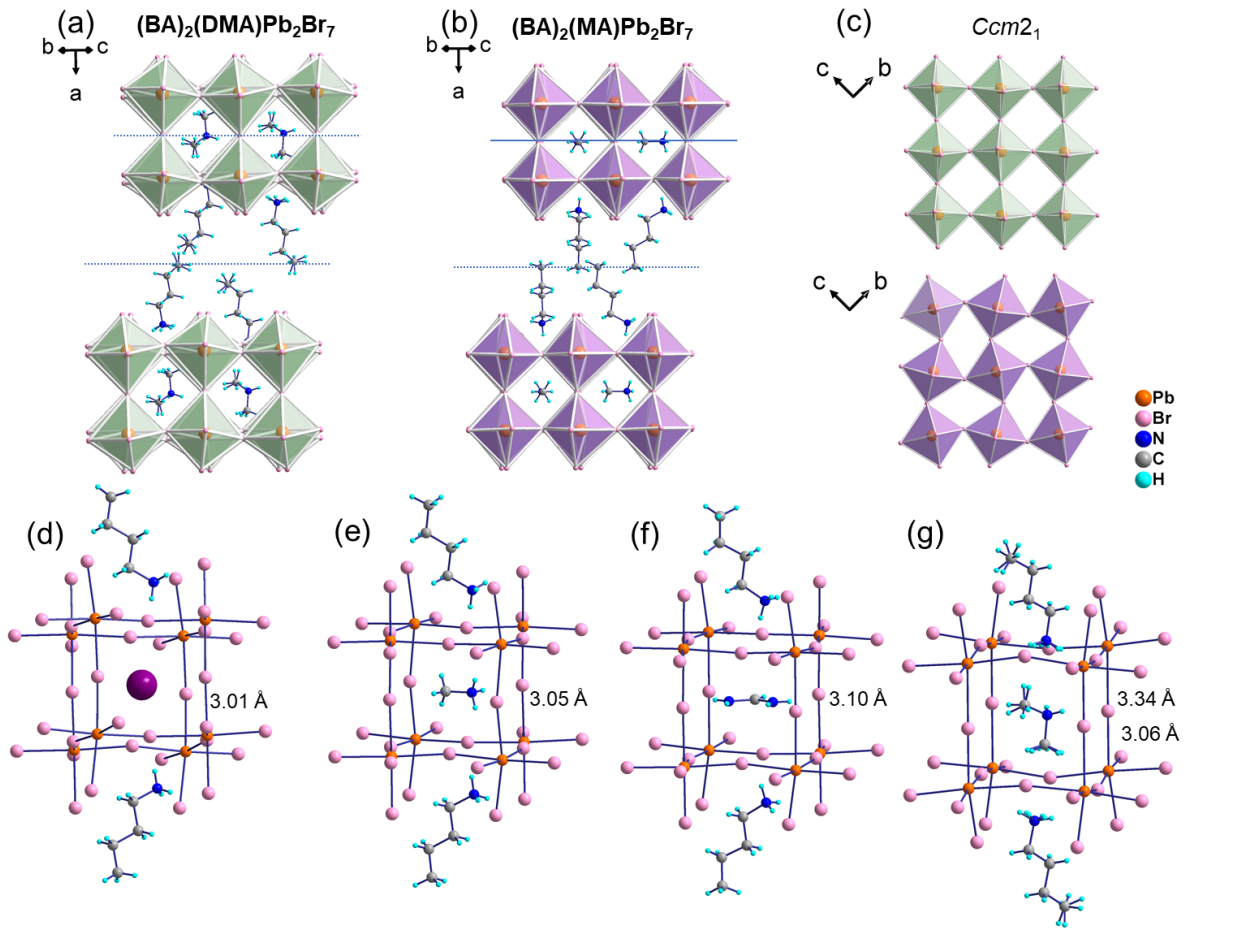


Figure 3. Comparison of crystal structures for (a) $(BA)_2(DMA)Pb_2Br_7$ and (b) $(BA)_2(MA)Pb_2Br_7$ from the side view, (c) from the top view. Crystal structures of (d) $(BA)_2(Cs)Pb_2Br_7$, (e) $(BA)_2(MA)Pb_2Br_7$, (f) $(BA)_2(FA)Pb_2Br_7$ and (g) $(BA)_2(DMA)Pb_2Br_7$ emphasizing the perovskite cage.

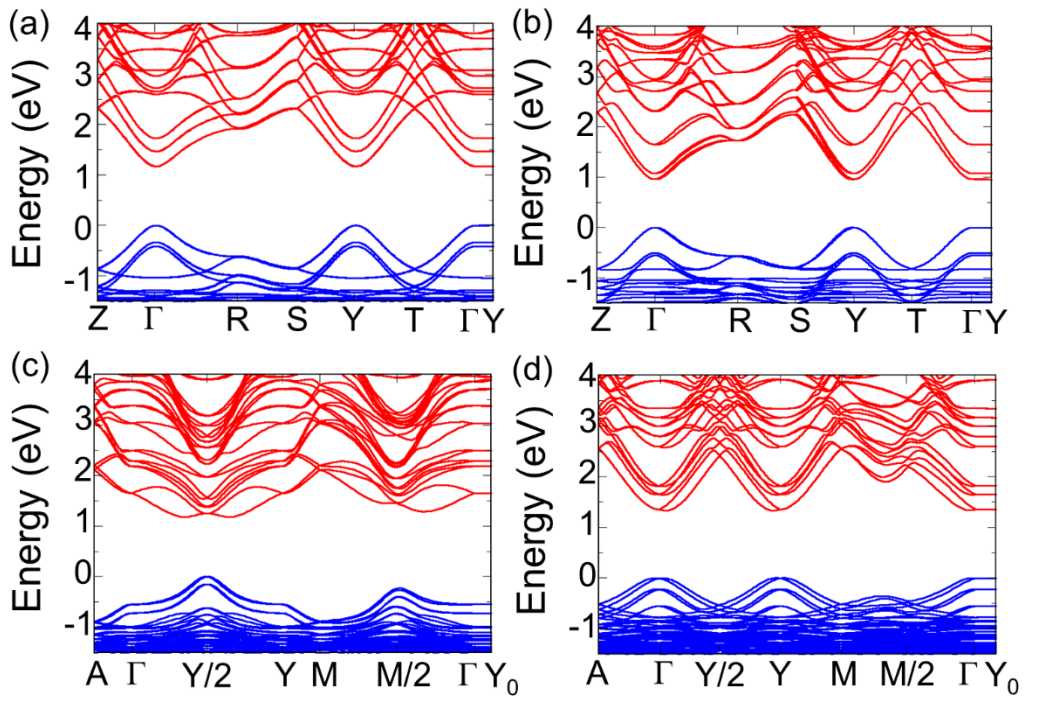


Figure 4. Electronic band structures of (a) $(BA)_2(Cs)_2Pb_3Br_{10}$, (b) $(BA)_2(MA)_2Pb_3Br_{10}$, (c) $(BA)_2(MHy)_2Pb_3Br_{10}$ and (d) $(BA)_2(EA)_2Pb_3Br_{10}$.

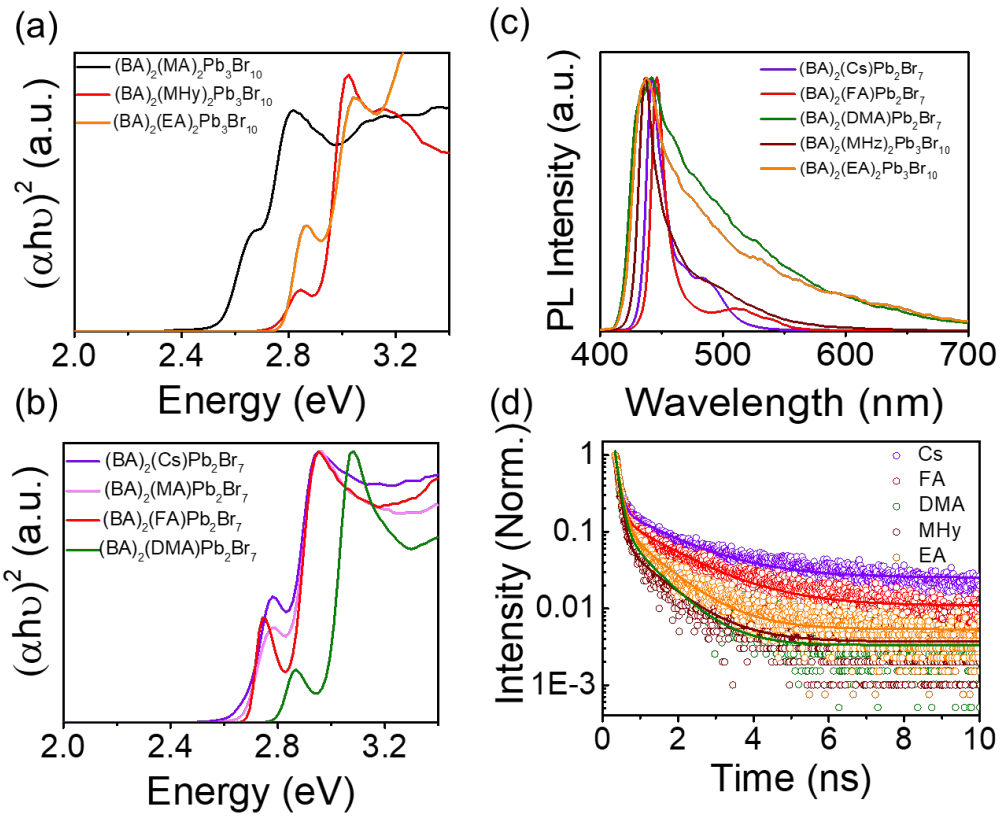


Figure 5. Tauc plots of the absorption spectra for the (a) n = 3 compounds and (b) n = 2 compounds. (c) PL spectra of the compounds. (d) PL decay curves.

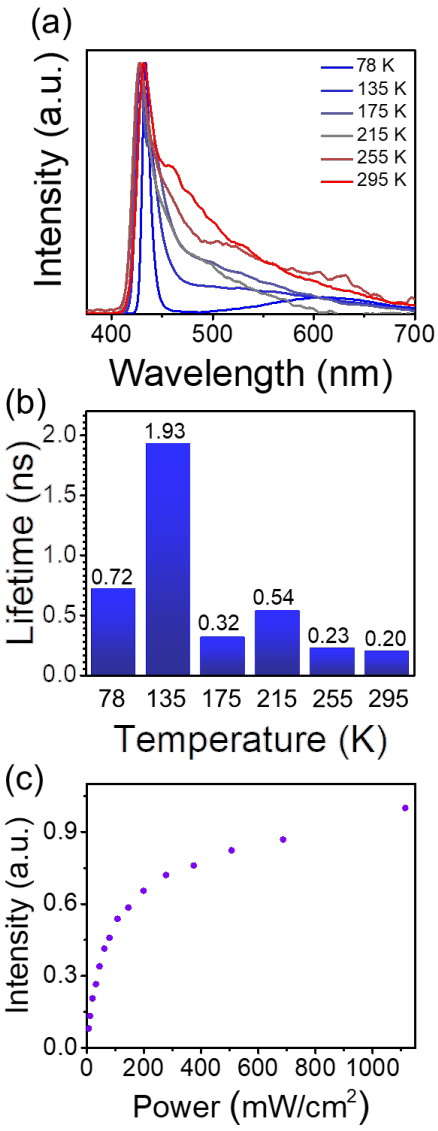


Figure 6. (a) Temperature-dependent PL spectra, (b) PL lifetimes of $(BA)_2(EA)_2Pb_3Br_{10}$ at different temperatures. (c) PL intensity versus excitation power for $(BA)_2(EA)_2Pb_3Br_{10}$ at room temperature.

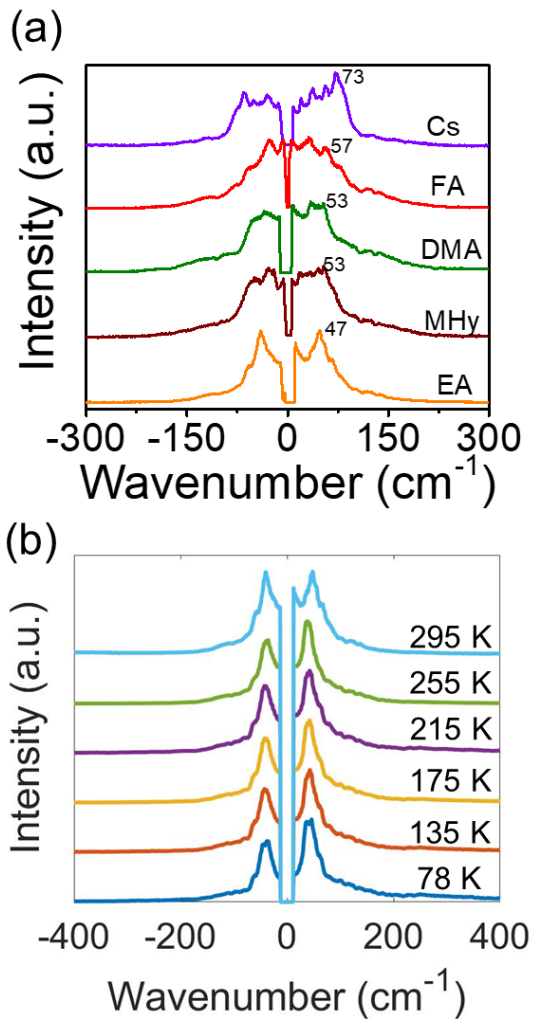


Figure 7. (a) Room-temperature low-frequency Raman spectra for the compounds. (b) Temperature-dependent Raman spectra of $(BA)_2(EA)_2Pb_3Br_{10}$.The numbers in Figure 7(a) indicate the frequencies of the main peaks in $cm^{-1}$.

# Supporting Information

## Expanding the Cage of 2D Bromide Perovskites by Large A-site Cations

Xiaotong Li,[†] Shelby A. Cuthriell,[†] Ashanti Bergonzoni, [‖] Hao Dong, [‡] Boubacar Traoré,[§] Constantinos C. Stoumpos,[▽] Peijun Guo, [‡] Jacky Even,[‖] Claudine Katan,[§] Richard D. Schaller,[†, ◊] and Mercouri G. Kanatzidis[*,†]

[†]Department of Chemistry, Northwestern University, 2145 Sheridan Road, Evanston, Illinois 60208, United States
[‖]Univ Rennes, INSA Rennes, CNRS, Institut FOTON, UMR 6082, Rennes F-35000, France
[‡]Department of Chemical and Environmental Engineering, Yale University, New Haven, Connecticut 06511, United States
[§]Univ Rennes, ENSCR, INSA Rennes, CNRS, ISCR (Institut des Sciences Chimiques de Rennes), UMR 6226, Rennes F-35000, France
[▽]Department of Materials Science and Technology, Voutes Campus, University of Crete, Heraklion GR-70013, Greece
[◊]Center for Nanoscale Materials, Argonne National Laboratory, 9700 South Cass Avenue, Lemont, Illinois 60439, United States

**Starting Materials** $PbBr_2$ (98%), methylamine hydrochloride (98%), formamidine acetate (99%), dimethylamine hydrochloride (99%), methylhydrazine (98%), ethylammonium chloride (98%), hydrobromic acid (48 wt % in $H_2O$, distilled, stabilized, 99.95%), and hypophosphorous acid solution (50 wt % in $H_2O$) were purchased from Sigma-Aldrich and used as received.

**Synthesis of $(BA)_2(MA)_2Pb_3Br_{10}$.** We used the ingredients ratio reported in the literature,[1] where a slow cooling method with a rate of 0.5 °C/day was used. But this cannot be achieved with our furnace, so we used a direct cooling method instead, which might be the origin of the higher layer-number. But the position of the absorption edge matches with that reported in the literature.

**Powder X-ray Diffraction.** Powder X-ray diffraction analysis was performed using a Rigaku Miniflex600 powder X-ray diffractometer (Cu Kα graphite, λ = 1.5406 Å) operating at 40 kV/15 mA with a Kβ foil filter.

**Single Crystal Structure.** Single-crystal X-ray diffraction experiments were performed using a STOE IPDS II or IPDS 2T diffractometer with Mo Kα radiation (λ = 0.71073 Å) and operating at 50 kV and 40 mA. Integration and numerical absorption corrections were performed using the X-AREA, X-RED, and XSHAPE programs. The structures were solved by charge flipping and refined by full-matrix least-squares on $F^2$ using the Jana 2006 package.[2]

**Differential Scanning Calorimetry (DSC).** DSC measurements were performed with a TA Q200 instrument. 10 mg of each sample was placed in an aluminum crucible that was cold sealed with a press. Sample was measured under ultra-high purity nitrogen gas (50 ml/min) and an empty aluminum was used as a reference. Baseline signal, collected with no crucibles loaded in the cell, was subtracted automatically from the raw data. Temperature was increased at a rate of 5 ℃ /min from -80 ℃ to 150 ℃.

**Optical Absorption Spectroscopy.** Optical diffuse reflectance measurements were performed using a Shimadzu UV-3600 UV−vis NIR spectrometer operating in the 200−2500 nm region at room temperature. $BaSO_4$ was used as the reference of 100% reflectance for all measurements. The reflectance versus wavelength data generated were used to estimate the bandgap of the material by converting reflectance to absorption data according to the Kubelka−Munk equation: $\alpha/S = (1- R)^2(2R)^{-1}$, where R is the reflectance and α and S are the absorption and scattering coefficients, respectively. For temperature dependent Raman measurements, the samples were mounted in a liquid-nitrogen cryostat (Janis VPF-100) at a pressure below $10^{-4}$ Torr.

**Computational details:** First-principles calculations were based on density functional theory (DFT)[3,4] as implemented in the SIESTA package[5] with a basis set of finite-range of numerical atomic orbitals[6]. The calculations were performed experimental structures, after transformation into their primitive cells whenever relevant. The positions of hydrogen atoms were optimized for all compounds using the van der Waals density functional of Dion et al. corrected by Cooper (C09)[7,8]. For the electronic structure computations, single-point calculations were conducted within the Generalized Gradient Approximation (GGA) using Perdew-Burke-Ernzerhof (PBE) functional[9] as the exchange-correlation term. Norm-conserving Troullier-Martins pseudopotentials[10] were used to account for the core electrons while $1s^1$, $2s^22p^2$, $2s^22p^3$, $5p^66s^1$, $4s^24p^5$, and $6s^26p^25d^{10}$ were considered as valence electrons for H, C, N, Cs, Br and Pb, respectively. Double-Zeta Polarized (DZP) basis sets with an energy shift of 200 meV were used for the valence atomic orbitals. A mesh cutoff of 300 Rydberg was adopted for the real space grid. The different Brillouin zones were sampled with a 3*3*6 and 4*4*4 Monckhorst-Pack grids for the 2D compounds and 3D compounds respectively. Spin-orbit coupling (SOC), when used, was considered in its fully relativistic spin-DFT formalism. The effective masses were extracted under the parabolic approximation of the bands near the band extrema.

**Photoluminescence.** Photoluminescence spectra, PXRD and absorption spectra were measured using the same polycrystalline samples. A 375 nm ps laser (Picoquant LDH-D-C-375) was used as the excitation source running at a 10 MHz repetition rate. A long-working-distance objective (Mitutoyo, 10X, NA=0.28) was used to focus the laser onto the samples and collect the PL signal. The samples were mounted in a liquid-nitrogen cryostat (Janis VPF-100) at a pressure below $10^{-4}$ Torr. A dichroic mirror was placed on the path to block the reflected laser light, and a 400 nm long-pass filter was placed near the entrance slit of the spectrograph (Andor Kymera 328i) to further reject any residual laser light. Time-integrated PL spectra was captured by a Si EMCCD (Andor iXon Life 888), and time-resolved PL was collected by a streak camera (Hamamatsu C10910 with the Slow sweep unit; M10913).

**Raman Spectra.** Low-frequency Raman spectra were measured using a frequency-stabilized 785 nm laser (Toptica) as the excitation source with an incident power of 40 mW onto the sample. A set of 5 narrow-linewidth notch filters (OptiGrate) was used to reject the laser line and enable measurements of Raman signatures down to 5 $cm^{-1}$. A super-long-working-distance objective lens

(10X, NA=0.28) was used to focus the excitation light and to collect the Raman signal. The Raman signal was spatially filtered by a pair of 75-mm achromatic lens and a 50-μm pinhole, before sent into the spectrograph (Andor Kymera 328i). The Raman signal was finally captured by a Si EMCCD (Andor iXon Life 888).

Table S1. Atomic coordinates ($x10^4$) and equivalent isotropic displacement parameters ($Å^2x10^3$) for $(BA)_2(MHy)_2Pb_3Br_{10}$ at 293 K with estimated standard deviations in parentheses.

| Label | x | y | z | Occupancy | $U_{eq}^*$ |
|---|---|---|---|---|---|
| Pb(1) | 4914(1) | -48(3) | 3201(1) | 1 | 34(1) |
| Pb(2) | 7305(1) | -52(3) | 4395(1) | 1 | 34(1) |
| Pb(3) | 6111(1) | 907(2) | 3607(1) | 1 | 36(1) |
| Br(1) | 5525(1) | -135(9) | 3548(1) | 1 | 71(2) |
| Br(2) | 6112(1) | -1145(5) | 1349(1) | 1 | 73(2) |
| Br(3) | 6694(1) | -142(9) | 4133(1) | 1 | 65(2) |
| Br(4) | 6110(1) | -4043(6) | 4411(1) | 1 | 75(2) |
| Br(5) | 7285(1) | -64(11) | 6887(1) | 1 | 105(3) |
| Br(6) | 4937(1) | 65(11) | 715(1) | 1 | 107(3) |
| Br(7) | 7300(1) | -5062(9) | 4297(1) | 1 | 104(3) |
| Br(8) | 4925(1) | -5067(9) | 3109(1) | 1 | 98(3) |
| Br(9) | 4361(1) | -80(20) | 3060(1) | 1 | 199(7) |
| Br(10) | 7858(1) | -50(20) | 4827(1) | 1 | 190(6) |

Table S2. Anisotropic displacement parameters ($Å^2x10^3$) for $(BA)_2(MHy)_2Pb_3Br_{10}$ at 293 K with estimated standard deviations in parentheses.

| Label | $U_{11}$ | $U_{22}$ | $U_{33}$ | $U_{12}$ | $U_{13}$ | $U_{23}$ |
|---|---|---|---|---|---|---|
| Pb(1) | 55(1) | 24(1) | 25(1) | -3(1) | 12(1) | -1(1) |
| Pb(2) | 55(1) | 24(1) | 24(1) | 3(1) | 8(1) | 1(1) |
| Pb(3) | 51(1) | 29(1) | 29(1) | 0(1) | 10(1) | 0(1) |
| Br(1) | 70(4) | 73(3) | 75(3) | -12(3) | 25(2) | 4(2) |
| Br(2) | 161(4) | 28(2) | 32(2) | -5(3) | 24(2) | -1(2) |
| Br(3) | 44(3) | 72(3) | 77(2) | 8(2) | -2(2) | 6(2) |
| Br(4) | 170(5) | 21(2) | 37(2) | 1(2) | 24(2) | 4(2) |
| Br(5) | 198(7) | 93(4) | 29(2) | 3(4) | 25(3) | -6(2) |

| | | | | | | |
|---|---|---|---|---|---|---|
| Br(6) | 194(7) | 102(4) | 30(2) | 5(4) | 31(3) | 7(2) |
| Br(7) | 187(6) | 26(2) | 114(3) | 4(4) | 90(3) | -1(3) |
| Br(8) | 181(7) | 24(2) | 80(3) | -5(4) | -28(3) | -1(2) |
| Br(9) | 66(6) | 231(15) | 296(12) | 19(7) | 2(7) | 11(9) |
| Br(10) | 46(5) | 227(14) | 292(11) | -14(6) | -3(6) | -6(8) |

Table S3. Atomic coordinates ($x10^4$) and equivalent isotropic displacement parameters ($Å^2x10^3$) for $(BA)_2(EA)_2Pb_3Br_{10}$ at 293 K with estimated standard deviations in parentheses.

| Label | x | y | z | Occupancy | $U_{eq}^*$ |
|---|---|---|---|---|---|
| Pb(1) | -7865(1) | -2511(2) | -6421(1) | 1 | 48(1) |
| Pb(2) | -6627(1) | -2615(1) | -6665(1) | 1 | 42(1) |
| Pb(3) | -5389(1) | -2509(2) | -6423(1) | 1 | 48(1) |
| Br(1) | -6043(1) | -2289(4) | -6415(1) | 1 | 74(2) |
| Br(2) | -7812(1) | 38(3) | -8883(1) | 1 | 76(2) |
| Br(3) | -7214(1) | -2274(3) | -6410(1) | 1 | 73(2) |
| Br(4) | -7956(1) | -5055(3) | -8873(1) | 1 | 79(2) |
| Br(5) | -8398(1) | -1893(5) | -6435(1) | 1 | 115(2) |
| Br(6) | -5439(1) | 37(3) | -8888(1) | 1 | 81(2) |
| Br(7) | -5297(1) | -4952(3) | -3879(1) | 1 | 80(2) |
| Br(8) | -4850(1) | -1896(5) | -6446(1) | 1 | 112(2) |
| Br(9) | -6627(1) | -5644(3) | -8637(1) | 1 | 69(1) |
| Br(10) | -6626(1) | -376(2) | -9640(1) | 1 | 61(1) |

Table S4. Anisotropic displacement parameters ($Å^2x10^3$) for $(BA)_2(EA)_2Pb_3Br_{10}$ at 293 K with estimated standard deviations in parentheses.

| Label | $U_{11}$ | $U_{22}$ | $U_{33}$ | $U_{12}$ | $U_{13}$ | $U_{23}$ |
|---|---|---|---|---|---|---|
| Pb(1) | 66(1) | 36(1) | 42(1) | 3(1) | -1(1) | -1(1) |
| Pb(2) | 53(1) | 36(1) | 37(1) | -1(1) | 0(1) | 0(1) |
| Pb(3) | 63(1) | 37(1) | 42(1) | -1(1) | 1(1) | -1(1) |
| Br(1) | 49(2) | 90(2) | 84(2) | 7(2) | 0(2) | 7(2) |
| Br(2) | 115(3) | 56(2) | 56(2) | -2(2) | -5(2) | 21(2) |
| Br(3) | 69(2) | 70(2) | 79(2) | 3(2) | 3(2) | 2(2) |
| Br(4) | 131(3) | 55(2) | 53(2) | -11(2) | 6(2) | -16(2) |
| Br(5) | 68(3) | 72(2) | 206(3) | -2(3) | 2(2) | 2(2) |

| | | | | | | |
|---|---|---|---|---|---|---|
| Br(6) | 133(3) | 54(2) | 55(2) | 5(2) | 5(2) | 19(2) |
| Br(7) | 131(3) | 56(2) | 54(2) | -12(2) | -6(2) | 15(2) |
| Br(8) | 51(3) | 77(2) | 207(3) | -5(2) | -4(2) | -3(2) |
| Br(9) | 88(2) | 58(2) | 60(2) | -1(2) | 0(2) | -23(1) |
| Br(10) | 78(2) | 50(2) | 54(1) | -2(2) | 2(2) | 11(1) |

Table S5. Atomic coordinates ($x10^4$) and equivalent isotropic displacement parameters ($Å^2x10^3$) for $(BA)_2(DMA)Pb_2Br_7$ at 293 K with estimated standard deviations in parentheses.

| Label | x | y | z | Occupancy | $U_{eq}^*$ |
|---|---|---|---|---|---|
| Pb(1) | 6693(1) | 0 | 2602(1) | 1 | 49(1) |
| Pb(2) | 8308(1) | 0 | 2600(1) | 1 | 51(1) |
| Br(1) | 5982(2) | 0 | 2049(2) | 1 | 137(5) |
| Br(2) | 8417(1) | -2593(7) | 118(2) | 1 | 103(1) |
| Br(3) | 9015(2) | 0 | 3165(2) | 1 | 112(3) |
| Br(4) | 6746(1) | -2570(10) | 96(2) | 1 | 99(1) |
| Br(5) | 7533(2) | 0 | 2595(2) | 1 | 135(2) |

Table S6. Anisotropic displacement parameters ($Å^2x10^3$) for $(BA)_2(DMA)Pb_2Br_7$ at 293 K with estimated standard deviations in parentheses.

| Label | $U_{11}$ | $U_{22}$ | $U_{33}$ | $U_{12}$ | $U_{13}$ | $U_{23}$ |
|---|---|---|---|---|---|---|
| Pb(1) | 76(1) | 35(1) | 35(1) | 0 | -7(1) | 0 |
| Pb(2) | 74(1) | 44(1) | 36(1) | 0 | 4(1) | 0 |
| Br(1) | 53(3) | 240(13) | 119(4) | 0 | -18(3) | 0 |
| Br(2) | 185(2) | 59(2) | 63(1) | 35(3) | -37(2) | -28(1) |
| Br(3) | 82(4) | 196(9) | 56(2) | 0 | 16(2) | 0 |
| Br(4) | 168(2) | 64(2) | 65(1) | -9(4) | 10(3) | -34(1) |
| Br(5) | 48(2) | 195(4) | 164(3) | 0 | -12(2) | 0 |

Table S7. Comparison of Pb-Br bond lengths for the n = 3 phases.

| Compound | $(BA)_2(Cs)_2Pb_3Br_{10}$ | $(BA)_2(MA)_2Pb_3Br_{10}$ | $(BA)_2(MHy)_2Pb_3Br_{10}$ | $(BA)_2(EA)_2Pb_3Br_{10}$ |
|---|---|---|---|---|
| **Equatorial Pb−Br (Å)** | 2.9561(14) | 2.983(2) | 2.9639(15) | 3.009(2) |
| | 2.9560(14) | 2.979(3) | 2.9690(14) | 3.013(2) |
| | 2.965(3) | 3.027(3) | 2.996(5) | 3.025(2) |
| | 2.943(4) | 3.034(2) | 2.973(5) | 3.017(2) |
| | 2.949(4) | 2.953(2) | 2.9683(15) | 3.058(2) |
| | 2.943(4) | 2.967(2) | 2.9639(14) | 2.9557(15) |
| | 2.965(3) | 2.9903(19) | 2.990(6) | 3.1488(16) |
| | 2.965(3) | 2.992(2) | 2.978(6) | 3.058(2) |
| | 2.9926(15) | 2.953(2) | 2.9441(18) | 3.007(2) |
| | 2.967(3) | 2.967(2) | 3.2528(15) | 3.008(2) |
| | 2.950(3) | 2.9903(19) | 3.102(4) | 3.021(2) |
| | 2.967(3) | 2.992(2) | 3.159(4) | 3.026(2) |
| **Axial Pb−Br (internal) (Å)** | 2.967(8) | 2.9766(8) | 3.118(4) | 2.9941(13) |
| | 2.967(8) | 2.9766(8) | 3.122(3) | 3.0148(14) |
| | 2.967(5) | 3.1021(8) | 3.069(4) | 3.3191(15) |
| | 2.967(5) | 3.1021(8) | 3.055(3) | 3.3392(15) |
| **Axial Pb−Br (external) (Å)** | 2.949(4) | 2.8912(10) | 2.830(4) | 2.7722(15) |
| | 2.949(4) | 2.8912(10) | 2.830(4) | 2.7934(15) |
| **Ave eq Pb−Br (Å)** | 2.960(3) | 2.986(2) | 3.022(3) | 3.029(2) |
| **Ave ax (int) Pb−Br (Å)** | 2.967(7) | 3.039(1) | 3.091(4) | 3.167(1) |
| **Ave ax (ext) Pb−Br (Å)** | 2.949(4) | 2.891(1) | 2.830(4) | 2.783(2) |
| **Ave Pb-Br (Å)** | 2.960(4) | 2.987(2) | 3.016(4) | 3.032(2) |

Table S8. Comparison of Pb-Br-Pb bond angles for the n = 3 phases.

| Compound | $(BA)_2(Cs)_2Pb_3Br_{10}$ | $(BA)_2(MA)_2Pb_3Br_{10}$ | $(BA)_2(MHy)_2Pb_3Br_{10}$ | $(BA)_2(EA)_2Pb_3Br_{10}$ |
|---|---|---|---|---|
| Equatorial Pb-Br-Pb (°) | 154.79 | 161.68 | 175.23 | 169.54 |
| | 152.85 | 163.59 | 175.11 | 162.20 |
| | 152.69 | 167.53 | 175.66 | 152.95 |
| | 155.46 | 155.13 | 175.52 | 161.07 |
| | | | 152.94 | 170.22 |
| | | | 144.54 | 162.11 |
| Axial Pb-Br-Pb (°) | 179.16 | 176.37 | 165.94 | 170.05 |
| | | | 165.76 | 170.54 |
| Ave eq Pb-Br-Pb (°) | 153.94 | 161.98 | 166.50 | 163.02 |
| Ave ax Pb-Br-Pb (°) | 179.16 | 176.37 | 165.85 | 170.30 |
| Ave Pb-Br-Pb (°) | 158.99 | 164.86 | 166.34 | 164.84 |

Table S9. Comparison of Pb-Br bond lengths and Pb-Br-Pb bond angles for the n = 2 phases.

| Compound | $(BA)_2(Cs)Pb_2Br_7$ | $(BA)_2(MA)Pb_2Br_7$ | $(BA)_2(FA)Pb_2Br_7$ | $(BA)_2(DMA)Pb_2Br_7$ |
|---|---|---|---|---|
| Equatorial Pb−Br (Å) | 2.958(2) | 2.9354(19) | 2.979(6) | 2.969(5) |
| | 2.9741(14) | 2.9914(14) | 2.993(5) | 3.052(6) |
| | 2.9990(14) | 2.9998(14) | 3.016(5) | 3.063(5) |
| | 3.0016(18) | 3.0324(17) | 3.022(6) | 2.932(6) |
| Axial Pb−Br (internal) (Å) | 3.0052(3) | 3.0472(3) | 3.1005(8) | 3.340(7)<br>3.063(7) |
| Axial Pb−Br (external) (Å) | 2.9758(10) | 2.9604(11) | 2.905(3) | 2.865(6)<br>2.837(6) |
| Ave eq Pb−Br (Å) | 2.983(2) | 2.990(2) | 3.003(5) | 3.004(6) |
| Ave ax Pb−Br (Å) | 2.991(1) | 3.004(1) | 3.003(2) | 3.026(7) |
| Ave Pb−Br (Å) | 2.986(1) | 2.994(1) | 3.003(4) | 3.011(6) |
| Bond Angles | | | | |
| Ave eq Pb−Br−Pb (°) | 156.2 | 155.7 | 162.6 | 167.4 |
| Ave ax Pb−Br−Pb (°) | 175.9 | 169.7 | 177.8 | 179.1 |
| Ave Pb−Br−Pb (°) | 162.8 | 160.4 | 167.7 | 171.3 |

Table S10. Summary of PL lifetimes and fitting parameters for $(BA)_2(EA)_2Pb_3Br_{10}$ at different temperatures.

| Temperature | $a_1$ | $\tau_1$ (ns) | $a_2$ | $\tau_2$ (ns) | $\tau_{ave}$ (ns) |
|---|---|---|---|---|---|
| 78 K | 0.85 | 0.24 | 0.15 | 1.26 | 0.72 |
| 135 K | 0.55 | 0.61 | 0.45 | 2.34 | 1.93 |
| 175 K | 0.96 | 0.17 | 0.04 | 0.92 | 0.32 |
| 215 K | 0.92 | 0.21 | 0.08 | 1.19 | 0.54 |
| 255 K | 0.98 | 0.13 | 0.02 | 0.87 | 0.23 |
| 295 K | 0.99 | 0.13 | 0.01 | 0.96 | 0.20 |

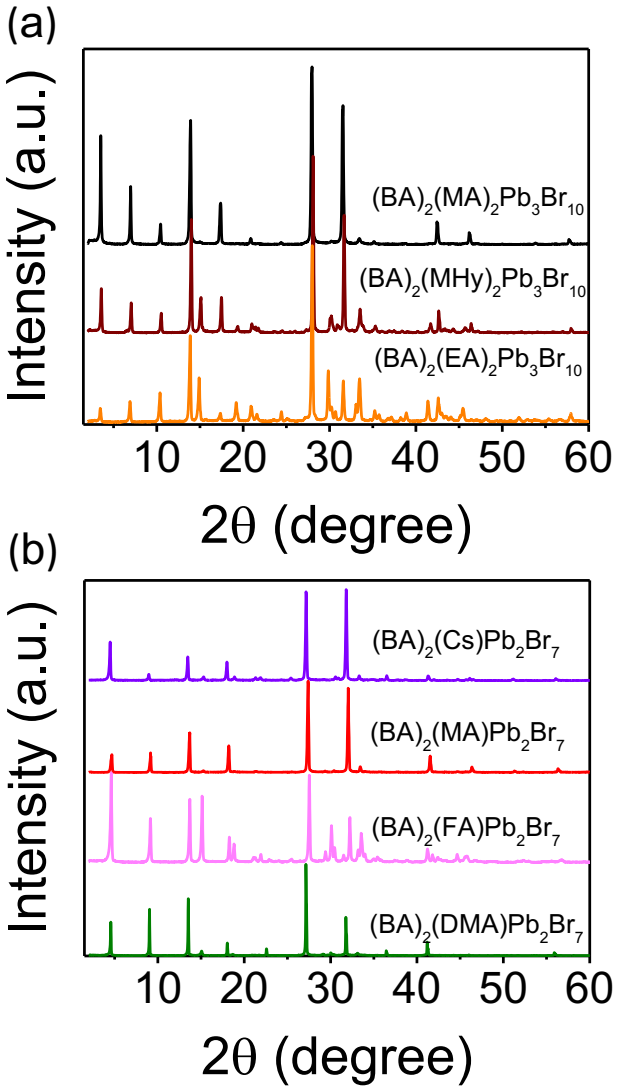


Figure S1. PXRD patterns of the (a) n = 3 phases and (b) n = 2 phases.

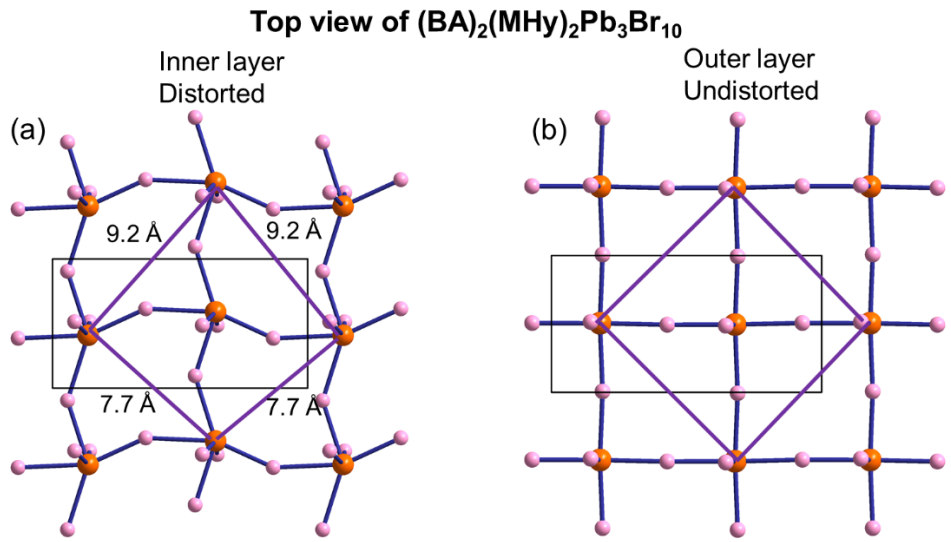


Figure S2. Individual layers of $(BA)_2(MHy)_2Pb_3Br_{10}$ from the top view. (a) Inner layer and (b) outer layer. The black lines indicate the unit cell.

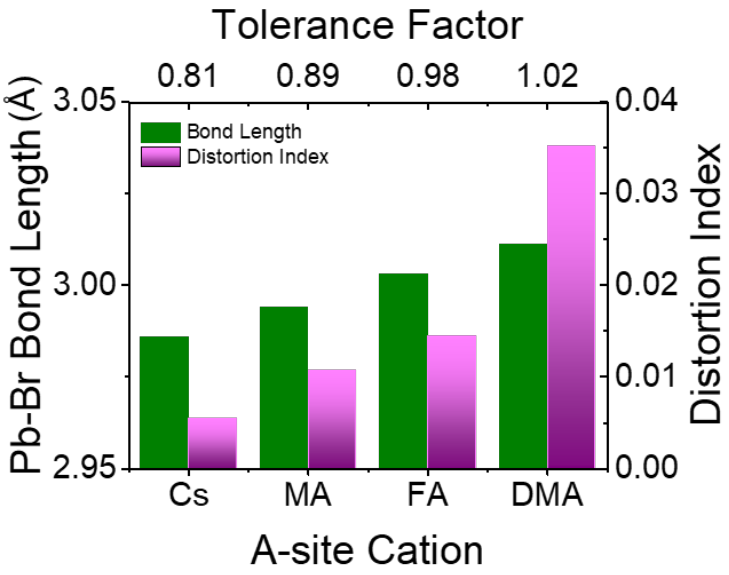


Figure S3. The relationships between the cation, tolerance factor, Pb-Br bond length and distortion index for n = 2 $(BA)_2(A)Pb_2Br_7$ phases.

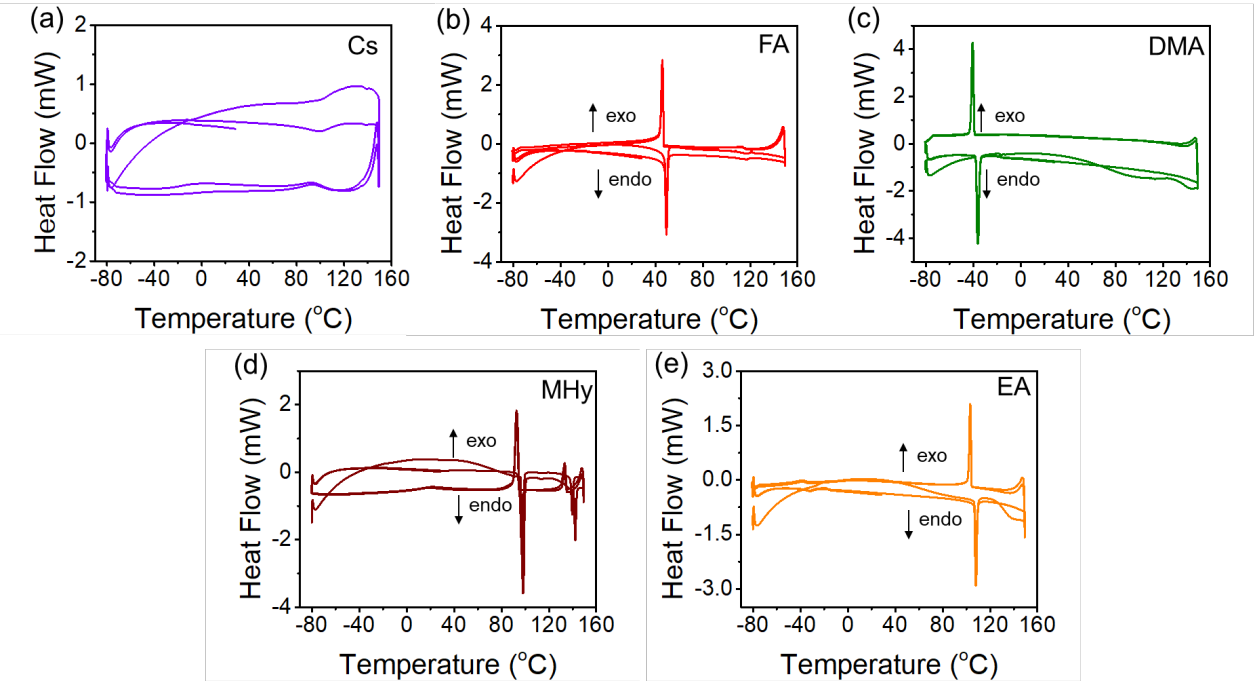


Figure S4. DSC curves of (a) $(BA)_2(Cs)Pb_2Br_7$, (b) $(BA)_2(FA)Pb_2Br_7$, (c) $(BA)_2(DMA)Pb_2Br_7$, (d) $(BA)_2(MHy)_2Pb_3Br_{10}$ and (e) $(BA)_2(EA)_2Pb_3Br_{10}$.

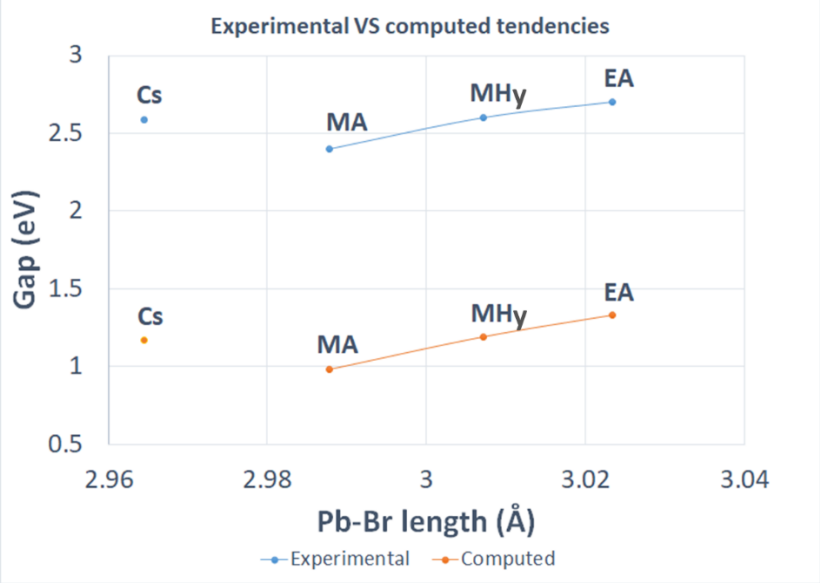


Figure S5. Experimental vs computed bandgaps for the n = 3 phases. The experimental bandgaps were extracted from the low-energy slope in Figure S4. The bandgap of Cs compound was extracted the same way from the literature.[11] However, the trend is the same as the numbers extracted from the high-energy slope: $E_{g,\,EA} > \approx E_{g,MHy} \approx E_{g,Cs} > E_{g,MA}$

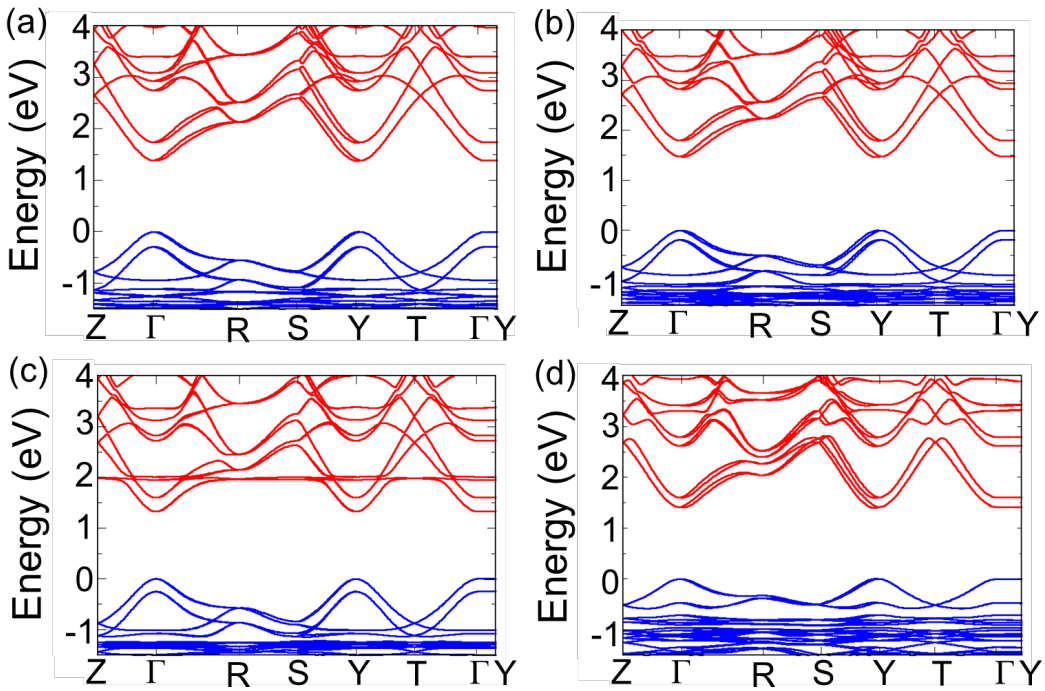


Figure S6. Electronic band structures of of (a) $(BA)_2(Cs)Pb_2Br_7$, (b) $(BA)_2(MA)Pb_2Br_7$, (c) $(BA)_2(FA)Pb_2Br_7$ and (d) $(BA)_2(DMA)Pb_2Br_7$.

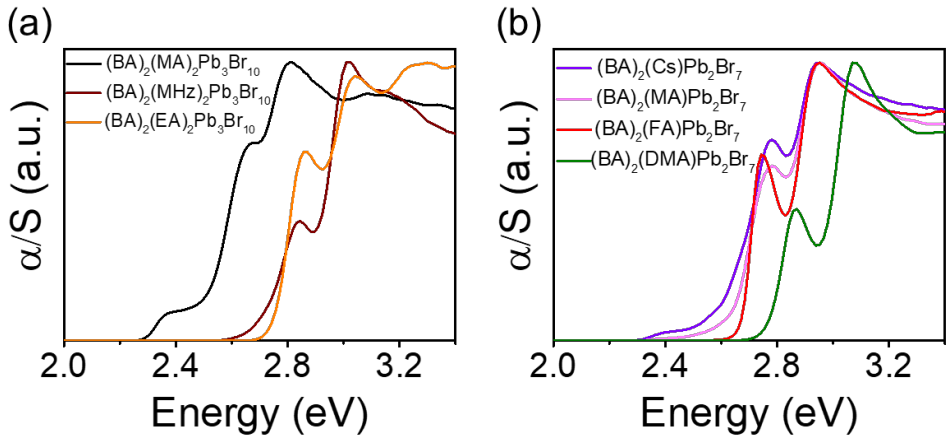


Figure S7. Absorption spectra of the (a) n = 3 and (b) n = 2 phases using Kubelka−Munk conversion from the diffuse-reflectance measurements of the grinded powders.

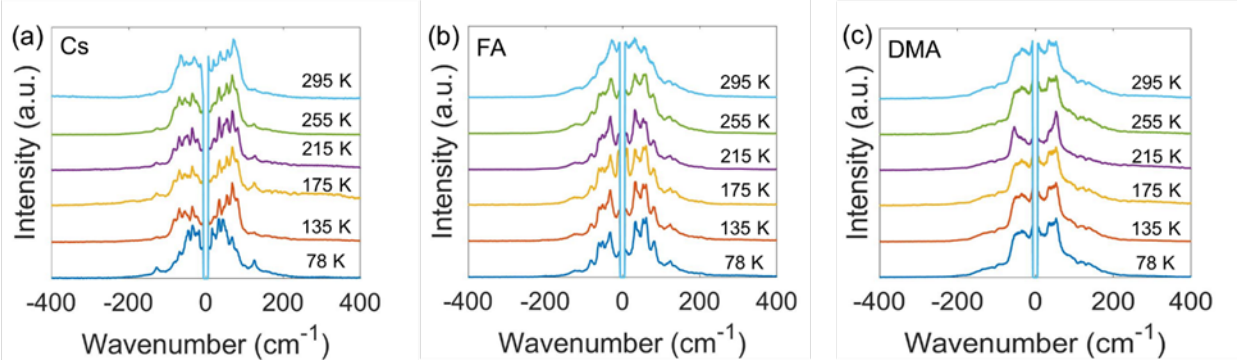


Figure S8. Temperature-dependent Raman spectra of (a) $(BA)_2(Cs)Pb_2Br_7$, (b) $(BA)_2(FA)Pb_2Br_7$ and (c) $(BA)_2(DMA)Pb_2Br_7$.

## References for SI

(1) Li, L.; Sun, Z.; Wang, P.; Hu, W.; Wang, S.; Ji, C.; Hong, M.; Luo, J., Tailored Engineering of an Unusual $(C_4H_9NH_3)_2(CH_3NH_3)_2Pb_3Br_{10}$ Two-Dimensional Multilayered Perovskite Ferroelectric for a High-Performance Photodetector. *Angew. Chem., Int. Ed.* **2017**, 56 (40), 12150-12154.

(2) Petříček, V.; Dušek, M.; Palatinus, L., Crystallographic Computing System JANA2006: General features. Z. Kristallogr. - Cryst. Mater. 2014, 229 (5), 345.

(3) Hohenberg, P.; Kohn, W. Inhomogeneous Electron Gas. *Phys. Rev.* **1964**, *136* (3B), B864–B871.

(4) Kohn, W.; Sham, L. J. Self-Consistent Equations Including Exchange and Correlation Effects. *Phys. Rev.* **1965**, *140* (4A), A1133–A1138.

(5) Soler, J. M.; Artacho, E.; Gale, J. D.; García, A.; Junquera, J.; Ordejón, P.; Sánchez-Portal, D. The SIESTA Method for *Ab Initio* Order- *N* Materials Simulation. *J. Phys. Condens. Matter* **2002**, *14* (11), 2745–2779.

(6) Junquera, J.; Paz, Ó.; Sánchez-Portal, D.; Artacho, E. Numerical Atomic Orbitals for Linear-Scaling Calculations. *Phys. Rev. B* **2001**, *64* (23), 235111.

(7) Dion, M.; Rydberg, H.; Schröder, E.; Langreth, D. C.; Lundqvist, B. I. Van Der Waals Density Functional for General Geometries. *Phys. Rev. Lett.* **2004**, *92* (24), 246401.

(8) Cooper, V. R. Van Der Waals Density Functional: An Appropriate Exchange Functional. *Phys. Rev. B* **2010**, *81* (16), 161104.

(9) Perdew, J. P.; Burke, K.; Ernzerhof, M. Generalized Gradient Approximation Made Simple. *Phys. Rev. Lett.* **1996**, *77* (18), 3865–3868.

(10) Troullier, N.; Martins, J. L. Efficient Pseudopotentials for Plane-Wave Calculations. *Phys. Rev. B* **1991**, *43* (3), 1993–2006.

(11) Chen, H.; Lin, J.; Kang, J.; Kong, Q.; Lu, D.; Kang, J.; Lai, M.; Quan, L. N.; Lin, Z.; Jin, J.; Wang, L.-w.; Toney, M. F.; Yang, P., Structural and spectral dynamics of single-crystalline Ruddlesden-Popper phase halide perovskite blue light-emitting diodes. *Sci. Adv.* **2020,** *6* (4), eaay4045.